

**AFRL-SN-RS-TR-1998-179**

**In-House Report**

**November 1998**



## **FIBER OPTIC BRAGG GRATINGS**

**James M. Battiato and Kent E. Hulick**

*APPROVED FOR PUBLIC RELEASE; DISTRIBUTION UNLIMITED.*

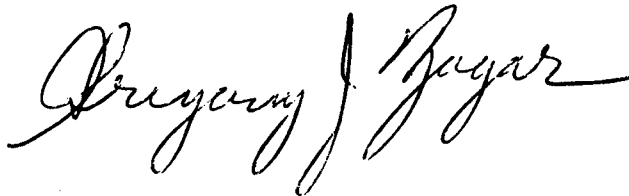
19990107 015

**AIR FORCE RESEARCH LABORATORY  
SENSORS DIRECTORATE  
ROME RESEARCH SITE  
ROME, NEW YORK**

This report has been reviewed by the Air Force Research Laboratory, Information Directorate, Public Affairs Office (IFOIPA) and is releasable to the National Technical Information Service (NTIS). At NTIS it will be releasable to the general public, including foreign nations.

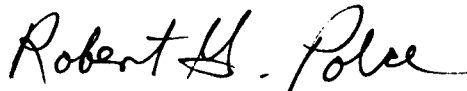
AFRL-SN-RS-TR-1998-179 has been reviewed and is approved for publication.

APPROVED:



GREGORY J. ZAGAR  
Chief, RF Photonics Branch  
Sensors Directorate

FOR THE DIRECTOR:



ROBERT G. POLCE  
Acting Chief, Rome Operations Office  
Sensors Directorate

If your address has changed or if you wish to be removed from the Air Force Research Laboratory Rome Research Site mailing list, or if the addressee is no longer employed by your organization, please notify AFRL/SNDR, 25 Electronic Parkway, Rome, NY 13441-4515. This will assist us in maintaining a current mailing list.

Do not return copies of this report unless contractual obligations or notices on a specific document require that it be returned.

REPORT DOCUMENTATION PAGE			Form Approved OMB No. 0704-0188	
<small>Public reporting burden for this collection of information is estimated to average 1 hour per response, including the time for reviewing instructions, searching existing data sources, gathering and maintaining the data needed, and completing and reviewing the collection of information. Send comments regarding this burden estimate or any other aspect of this collection of information, including suggestions for reducing this burden, to Washington Headquarters Services, Directorate for Information Operations and Reports, 1215 Jefferson Davis Highway, Suite 1204, Arlington, VA 22202-4302, and to the Office of Management and Budget, Paperwork Reduction Project (0704-0188), Washington, DC 20503.</small>				
1. AGENCY USE ONLY (Leave blank)		2. REPORT DATE November 1998		3. REPORT TYPE AND DATES COVERED In-House, Oct 95 - Jan 98
4. TITLE AND SUBTITLE  FIBER OPTIC BRAGG GRATINGS			5. FUNDING NUMBERS  PE - 62702F PR - 4600 TA - P1 WU - 22	
6. AUTHOR(S)  James M. Battiato and Kent E. Hulick				
7. PERFORMING ORGANIZATION NAME(S) AND ADDRESS(ES)  Air Force Research Laboratory/SNDR 25 Electronic Parkway Rome NY 13441-4515			8. PERFORMING ORGANIZATION REPORT NUMBER  AFRL-SN-RS-TR-1998-179	
9. SPONSORING/MONITORING AGENCY NAME(S) AND ADDRESS(ES)  Air Force Research Laboratory/SNDR 25 Electronic Parkway Rome NY 13441-4515			10. SPONSORING/MONITORING AGENCY REPORT NUMBER  AFRL-SN-RS-TR-1998-179	
11. SUPPLEMENTARY NOTES  Air Force Research Laboratory Project Engineer: James M. Battiato/SNDP/315-330-3142				
12a. DISTRIBUTION AVAILABILITY STATEMENT  APPROVED FOR PUBLIC RELEASE; DISTRIBUTION UNLIMITED.			12b. DISTRIBUTION CODE	
13. ABSTRACT (Maximum 200 words)  Coupled mode theory was used to model reflection fiber gratings. The effects of experimental parameters on grating characteristics were modeled for both uniform and non-uniform grating profiles using this approach. Fabrication of gratings in standard communication single mode fiber required an enhancement of the fiber's photosensitivity by way of high-pressure hydrogen treatment. The theory behind this technique as well as the experimental system used to treat the fibers was discussed. Once treated, the fibers were fabricated using a holographic approach. The performance of gratings fabricated by this method was then compared to theoretical predictions and was found to be in good agreement. Fiber grating shows great potential for use in RF photonic systems. Other in-house efforts are currently examining the use of fiber gratings in phased array radar beam steering systems.				
14. SUBJECT TERMS  Optical fiber, fiber gratings, fabrication, coupling, photosensitivity			15. NUMBER OF PAGES 76	
			16. PRICE CODE	
17. SECURITY CLASSIFICATION OF REPORT  UNCLASSIFIED	18. SECURITY CLASSIFICATION OF THIS PAGE  UNCLASSIFIED	19. SECURITY CLASSIFICATION OF ABSTRACT  UNCLASSIFIED	20. LIMITATION OF ABSTRACT  UL	

## TABLE OF CONTENTS

<b>Chapter 1</b> .....	1
1.1 Historical Background.....	2
1.2 Basic Concepts .....	3
1.3 Organization .....	5
<b>Chapter 2</b> .....	7
2.1 Dielectric Optical Waveguides.....	7
2.2 Modes of an Optical Fiber .....	10
2.2.1 LP Fiber Modes .....	14
2.3 Fiber Grating Calculations .....	17
2.3.1 Coupled Mode Equations .....	17
2.3.2 Uniform Fiber Bragg Grating.....	20
2.3.3 Non-uniform Gratings .....	28
2.4 Summary.....	33
<b>Chapter 3</b> .....	37
3.1 Photosensitivity in Optical Fibers .....	37
3.2 Hydrogen Loading.....	41
3.2.1 Hydrogen Loading System .....	45
3.3 Writing Technique.....	47
3.4 Reflection Fiber Gratings .....	49
3.4.1 Grating Period Calculation .....	50
3.4.2 Experimental Setup .....	53

3.4.3 Experimental Results.....	57
3.4.3.1 Uniform Grating .....	58
3.4.3.2 Non-uniform Grating.....	60
3.5 Summary.....	64
<b>Chapter 4.....</b>	<b>66</b>
4.1 Summary.....	66

## TABLE OF FIGURES

Figure 1-1	Two beam holographic exposure of the fiber core using the side writing technique.	4
Figure 2-1	Simple slab waveguide with cover, film, and substrate layers .....	7
Figure 2-2	Optical fiber waveguide consisting of a circular core surrounded by a lower index cladding .....	10
Figure 2-3	Calculated intensity plot of a $LP_{01}$ fiber mode and two dimensional cross section of a calculated $LP_{11}$ fiber mode .....	16
Figure 2-4	Sinusoidal index profile for a uniform fiber grating .....	21
Figure 2-5	Reflection spectra of a uniform fiber grating as a function of $\kappa L$ .....	24
Figure 2-6	Calculation of grating bandwidth as a function of coupling constant for the case of a weak grating.....	26
Figure 2-7	Calculation of grating bandwidth as a function of coupling constant for the case of a strong grating .....	27
Figure 2-8	Calculation of maximum grating reflectivity as a function of coupling constant ....	28
Figure 2-9	Non-uniform Gaussian index profile distribution .....	30
Figure 2-10	Reflection spectrum of a uniform grating calculated by both the closed form solution and numerically .....	34
Figure 2-11	Reflection spectrum of a fiber grating with a Gaussian index profile.....	35
Figure 3-1	Basic GeO defect structures .....	38
Figure 3-2	UV absorption spectrum of 3% mole germanium doped fiber perform before and after UV exposure.....	39
Figure 3-3	Normalized concentration of hydrogen gas diffused into the fiber as a function of radial position in the fiber.....	42
Figure 3-4	Normalized concentration of hydrogen in the core of the fiber as a function of time at 300 K and 294 K.....	44
Figure 3-5	Schematic of the hydrogen loading system consisting of two functional parts, the delivery system and the loading system .....	46

Figure 3-6	General methods used to create fiber grating utilizing the side writing technique ..	48
Figure 3-7	Bragg diagram for a non-slanted reflection grating.....	52
Figure 3-8	Experimental setup used for producing reflection fiber Bragg gratings .....	53
Figure 3-9	Transmission spectrum of a 1550 nm SOA used as a broadband source to measure fiber gratings.....	58
Figure 3-10	Measured and calculated transmission spectra for Bragg reflection in an 0.8mm long uniform grating with $\kappa L = 1.577$ .....	59
Figure 3-11	Measured transmission spectrum of a 4mm long fiber Bragg reflection with a Gaussian profile.....	61
Figure 3-12	Calculated transmission spectrum of a 4mm FWHM Gaussian index profile grating with $\sigma = 7 \times 10^{-4}$ , $\Delta = .0004$ , and $n_{\text{clad}} = 1.447$ .....	62
Figure 3-13	Shift in center wavelength of fiber grating from 827 nm to 829 nm with exposure time .....	63

## Chapter 1: Introduction

Since the first proposal by Kao and Hockham<sup>1</sup> on the feasibility of optical fiber in 1966 and the subsequent demonstration of these principles at Corning Glass Works in 1970<sup>2</sup>, the use of low loss optical fiber has rapidly evolved. The interest in, and massive growth of fiber optic systems has been spurred by the attractive properties offered by this medium. The advantages offered by fiber include low loss transmission, high bandwidth, small size, low weight, and immunity from external electromagnetic interference.

Concomitant with the growing interest and deployment of fiber optic systems is the development of components to be used in these systems. As a result, intense interest has focused on fiber Bragg gratings because of their ability to be used in many different applications. These applications include rare-earth doped fiber grating lasers,<sup>3</sup> dispersion compensation,<sup>4</sup> wavelength division multiplexing (WDM),<sup>5</sup> mode couplers,<sup>6</sup> wavelength stabilization of laser diodes,<sup>7</sup> hybrid fiber/semiconductor lasers,<sup>8</sup> fiber amplifier gain control,<sup>9</sup> grating based sensors,<sup>10</sup> time delay for phased array radar,<sup>11</sup> and nonlinear effect switches.<sup>12</sup>

It was the focus of this work unit to study fiber Bragg gratings and establish an in-house capability to fabricate fiber gratings for RF photonic applications.



## 1.1 Historical Background

The first fiber gratings were formed external to the core region. In these demonstrations the fiber cladding was side polished down close to the core and a grating was introduced by either placing a metallic grating on top of the polished region,<sup>13</sup> or by etching a grating directly into the polished surface.<sup>14</sup> These gratings interacted weakly with the evanescent field emerging from the core region and were challenging to fabricate. As a result, they were not very practical for real system applications. The many proposed applications inspired by these gratings, however, would later be revisited with the advent of in-core fiber gratings

The formation of a permanent grating written directly into the core of a fiber was first demonstrated by Ken Hill and co-workers at the Canadian Communications Research Centre in 1978.<sup>15</sup> They launched high intensity 488 nm radiation from an argon laser into a fiber and observed that the amount of light back reflected out of the fiber increased as a function of time, until almost all of the light transmitted through the fiber became depleted through back reflection. This type of grating, coined a “Hill grating”, was formed from the interference of counter propagating beams in the fiber core. Light transmitted through the fiber experienced a back reflection off the cleave at the end of the fiber. This back reflected light interfered with the input beam and the resulting standing wave pattern was recorded in the fiber core through a process later referred to as photosensitivity.

The formation of Hill Gratings was an unexplained curiosity until the important findings of Lam and Garside.<sup>16</sup> They reasoned that a two-photon process caused the grating formation and that gratings could be formed more efficiently if 244 nm radiation was used instead. This inspired Meltz and co-workers to holographically write a fiber grating with 244 nm radiation by exposing the fiber core to two interfering beams through the side of the fiber.<sup>17</sup> By varying the angle at which the writing beams intersected, fiber gratings could be made to act as Bragg reflectors at almost any wavelength.

## 1.2 Basic Concepts

Since the initial demonstration of fiber gratings, many approaches have been developed to write gratings directly into the core of the fiber (i.e. holographic, phase mask, prism, etc.). These are all similar in that they utilize the side writing technique. They vary in how they generate the interference pattern used to form the grating.

In this dissertation, the holographic approach was used because gratings of any fixed period could then be easily created. Fig. 1-1 illustrates the holographic side writing technique. A single coherent source is typically split into two beams by an interferometer. These beams are made to intersect at the fiber producing a periodic interference pattern that is recorded in the core as a refractive index modulation with period  $\Lambda$ . By changing the angle,  $\theta_B$ , at which they intersect, the period of the interference pattern and that of the resulting grating may be varied.

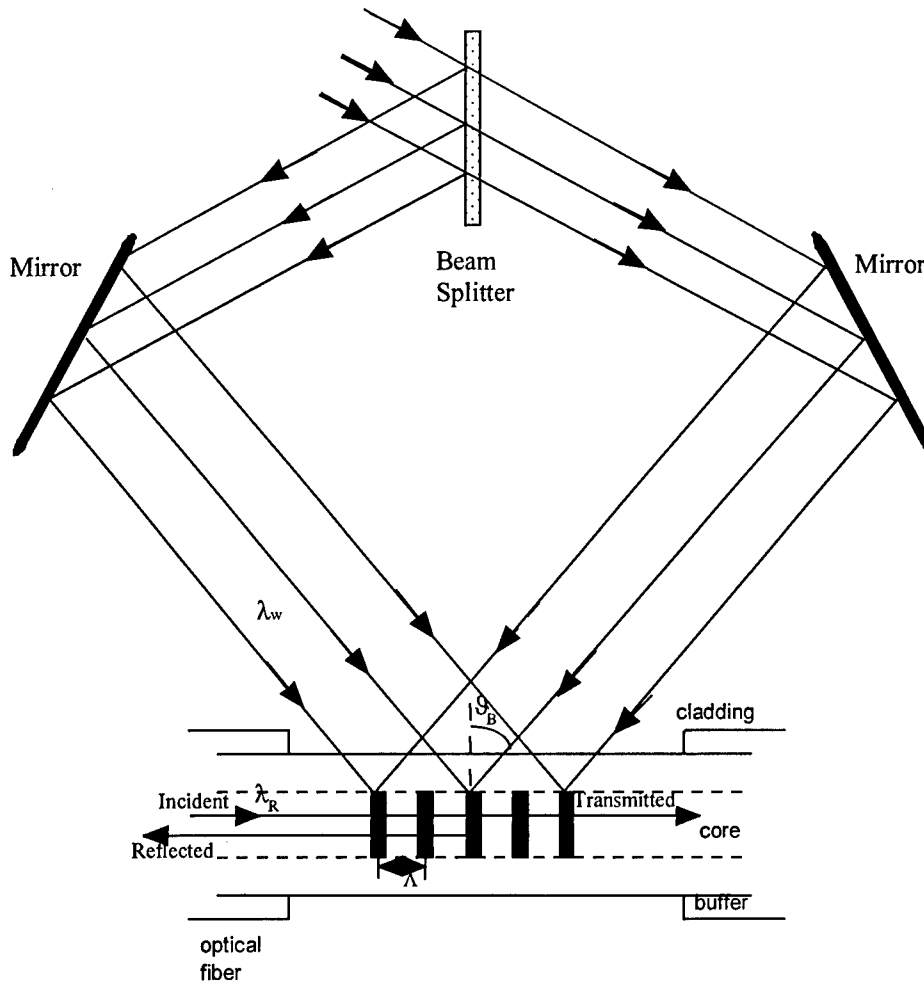


**Figure 1-1** Two beam holographic exposure of the fiber core using the side writing technique.

A signal traveling down the core of the fiber that has been exposed holographically as in Fig. 1-1 encounters a volume hologram where the writing beams overlapped. This signal will be diffracted if the Bragg condition is satisfied,

$$2n_{eff}\Lambda \sin \theta = m\lambda_B \quad 1-1$$

where  $n_{eff}$  is the effective index of the fiber mode,  $\theta$  is the angle of incidence on the grating,  $\Lambda$  is the period of the grating,  $m$  is the diffraction order, and  $\lambda_B$  is the grating wavelength. Eqn. 1-1 may be thought of as a phase matching condition that when satisfied implies that reflections from successive grating planes add coherently.

Reflection fiber Bragg gratings, as illustrated in Fig. 1-1, have fringe planes which are perpendicular to the fiber axis (non-tilted fringes). These gratings act as a wavelength dependent filters in a fiber. When the wavelength of the input beam matches the Bragg condition, the angle of incidence,  $\theta$ , equals the angle of diffraction and the beam is reflected back upon itself. The grating period for this case is given by,

$$\Lambda = \frac{\lambda_B}{2n_{eff}} . \quad 1-2$$

Fiber Bragg gratings can be characterized by their transmission or reflection spectra. These spectra may be measured in the lab with the aid of a broadband source and a spectrum analyzer or calculated by use of the coupled mode equations. The bandwidth and strength of these spectra are typically proportional to the length of the grating and the size of the induced index modulation.

### 1.3 Organization

This report is composed of four chapters, including this introduction. Chapter Two provides the background and theoretical models used to predict fiber grating performance. In Chapter Three, a discussion of fiber grating fabrication is presented as well as the experimental demonstration of different types of fiber gratings. Concluding comments are made in Chapter Four.

- 
- <sup>1</sup> K. C. Kao and G. A. Hockham, "Dielectric fiber surface waveguides for optical frequencies," *Proc. IEE*, vol. 133, pp. 1151-1158, 1966.
- <sup>2</sup> F. P. Kapron, D. B. Keck, and R. D. Maurer, "Radiation losses in glass optical waveguides," *Appl. Phys. Lett.*, vol. 17, pp. 423-425, 1970.
- <sup>3</sup> G. A. Ball, and W. W. Morey, "Continuously tunable single-mode erbium fiber laser," *Opt. Lett.*, vol. 17, pp. 420-422, 1992.
- <sup>4</sup> J. A. R. Williams, I. Bennion, K. Sugden, and N. J. Doran, "Fiber dispersion compensation using a chirped in-fibre Bragg grating," *Electron. Lett.*, vol. 30, pp. 985-987, 1994.
- <sup>5</sup> F. Bilodeau, K. O. Hill, B. Malo, D. C. Johnson, and J. Albert, "High-return-loss narrowband all-fiber bandpass Bragg transmission filter," *IEEE Photon. Technol. Lett.*, vol. 6, pp. 80-82, 1994.
- <sup>6</sup> K. O. Hill, B. Malo, K. A. Vineberg, F. Bilodeau, D. C. Johnson, and I. Skinner, "Efficient mode conversion in telecommunication fiber using externally written gratings," *Electron. Lett.*, vol. 26, pp. 1270-1272, 1990.
- <sup>7</sup> B. F. Ventrudo, G. A. Rodgers, G. S. Lick, D. Hargreaves, and T. N. Demayo, "Wavelength and intensity stabilization of 980 nm diode lasers coupled to fiber Bragg gratings," *Electron. Lett.*, vol. 30, pp. 2147-2149, 1994.
- <sup>8</sup> P. A. Morton, V. Mizrahi, S. G. Kosinski, L. F. Mollenauer, T. Tanbun-Ek, R. A. Logan, D. L. Coblenz, A. M. Sergent, and K. W. Wecht, "Hybrid soliton pulse source with fiber external cavity and Bragg reflector," *Electron. Lett.*, vol. 28, pp. 561-562, 1992.
- <sup>9</sup> J. Capmany, D. Pastor, and J. Marti, "EDFA gain equalizer employing linearly chirped apodized fiber gratings," *Microwave and Optic. Technol. Lett.*, vol. 12, pp. 158-160, 1996.
- <sup>10</sup> Eric Udd, editor, *Fiber Optic Sensors*, (Wiley, New York, 1991).
- <sup>11</sup> H. Zmuda, R. A. Soref, P. Payson, S. Johns, and E. N. Toughlian, "IEEE Photon. Technol. Lett.", vol. 9, pp. 241-243, 1997.
- <sup>12</sup> C. M. De Sterke, N. G. R. Broderick, B. J. Eggleton, and M. J. Steel, "Nonlinear optics in fiber gratings," *Optic. Fiber Technol.*, vol. 2, pp. 253-268, 1996.
- <sup>13</sup> W. V. Sorin and H. J. Shaw, "A Single Mode Fiber Evanescent Grating Reflector," *J. Lightwave Technol.*, vol. LT-3, pp. 1041-1043, 1985.
- <sup>14</sup> I. Bennion, D. C. Reid, C. J. Rowe, and W. J. Stewart, "High-Reflectivity Mono Mode-Fibre Grating Filters," *Electron. Lett.*, vol. 22, pp. 341-343, 1986.
- <sup>15</sup> K. O. Hill, Y. Fujii, D. C. Johnson, and B. S. Kawasaki, "Photosensitivity in optical fiber waveguides: Application to reflection filter fabrication," *Appl. Phys Lett.*, vol. 32, pp. 647-649, 1978.
- <sup>16</sup> D. K. W. Lam and B. K. Garside, "Characterization of single-mode optical fiber filters," *Appl. Opt.*, vol. 20, pp. 440-445, 1981.
- <sup>17</sup> G. Meltz, W. W. Morey, and W. H. Glenn, "Formation of Bragg gratings in optical fibers by a transverse holographic method," *Opt. Lett.*, vol. 14, pp. 823-825, 1989.

## Chapter 2: Theoretical Performance of Fiber Bragg Gratings

In this chapter the models used to predict the theoretical performance of fiber Bragg gratings are presented. Since most of theory is based on mode coupling, Section 2.1 provides a brief introduction into the basic principles of optical waveguides used throughout this chapter.

Section 2.2 deals specifically with optical fiber waveguides and defines the modes supported by a fiber. Finally in Section 2.3, these concepts are used to define and model fiber gratings.

### 2.1 Dielectric Optical Waveguides

An optical waveguide is a structure which guides light from one point to another. It is typically constructed with materials of different dielectric constants that are “stacked” perpendicular to the direction of propagation as illustrated in Fig. 2-1. Light propagation occurs in the guiding region of the waveguide through total internal reflection at the material interfaces. For this to occur, the guiding region must have a dielectric constant (and in turn an index of refraction) of greater value than the materials surrounding it.

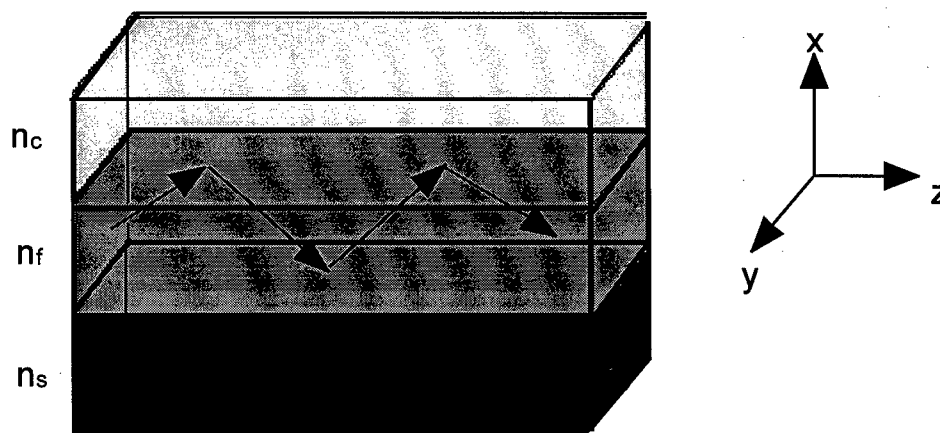


**Figure 2- 1** Simple slab waveguide with cover, film, and substrate layers and  $n_f > n_c \geq n_s$ . Light propagates in the longitudinal direction ( $z$ -direction) in the film layer via total internal reflection at each interface.

Following Koley's approach,<sup>1</sup> it is assumed that the electromagnetic fields in a waveguide have a periodic time dependence and can be written in the form,

$$\tilde{\mathbf{E}}(x, y, z, t) = \mathbf{E}(x, y, z)e^{i\omega t} + \mathbf{E}^*(x, y, z)e^{-i\omega t} \quad 2-1$$

$$\tilde{\mathbf{H}}(x, y, z, t) = \mathbf{H}(x, y, z)e^{i\omega t} + \mathbf{H}^*(x, y, z)e^{-i\omega t} \quad 2-2$$

where  $\mathbf{E}(x, y, z)$  and  $\mathbf{H}(x, y, z)$  are complex amplitudes. These amplitudes may be expressed in terms of their transverse (x,y-direction) and longitudinal(z-direction) components relative to the waveguide,

$$\mathbf{E}(x, y, z) = \mathbf{E}_t + \mathbf{E}_z \quad 2-3$$

$$\mathbf{H}(x, y, z) = \mathbf{H}_t + \mathbf{H}_z. \quad 2-4$$

Maxwell's equations are used to solve for the electro-magnetic fields propagating in an optical waveguide. Assuming a lossless media, Maxwell's equations can be written as

$$\nabla \times \mathbf{E}(x, y, z) = -i\omega\mu\mathbf{H}(x, y, z) \quad 2-5$$

$$\nabla \times \mathbf{H}(x, y, z) = i\omega\epsilon\mathbf{E}(x, y, z). \quad 2-6$$

In solving these equations boundary conditions must be satisfied at each material interface. If we assume that the waveguide in Fig. 2-1 is uniform in the longitudinal direction and changes only in the transverse direction, the resulting solutions must satisfy a transverse boundary-value problem. A waveguide mode is a field solution to this problem defined as

$$\mathbf{E}(x, y, z) = \mathbf{E}_v(x, y)e^{-i\beta_v z} \quad 2-7$$

$$\mathbf{H}(x, y, z) = \mathbf{H}_v(x, y)e^{-i\beta_v z} \quad 2-8$$

where the subscript v denotes the mode label and  $\beta_v$  is the propagation coefficient of the mode. Every distinct mode v has an eigenvalue  $\beta_v$  and a unique field distribution.

In general there are two basic types of solutions, guided modes and radiation modes. Guided modes are a set of solutions that are confined near the axis of the waveguide and form a set of discrete  $\beta$ 's. Radiation modes, on the other hand, form a continuum of values of  $\beta$  and radiate out of the guiding region.

An important characteristic of the modes is orthogonality. This means that modes are independent and do not interact with each other as they propagate. For guided modes this requires[1],

$$\iint (\mathbf{E}_i(x, y, z) \times \mathbf{E}_j^*(x, y, z))_z dx dy = \frac{2\omega\mu}{\beta_j} P \delta_{ij} . \quad 2-9$$

where  $P$  is the power carried by the mode and  $\delta_{ij}$  is the Kroenecker delta function ( $\delta_{ij}=1$  for  $i=j$ :  $\delta_{ij}=0$  otherwise).

An important consequence of mode orthogonality is that any arbitrary field distribution in the waveguide can be written as a superposition of waveguide modes. For an arbitrary field propagating in the  $z$ -direction, the transverse component may be written as

$$\mathbf{E}_t(x, y) = \sum_{\mu} a_{\mu} \mathbf{E}_{\mu}(x, y) e^{-i\beta_{\mu} z} . \quad 2-10$$

The ability to represent an arbitrary field as an expansion of waveguide modes is an important tool used in the coupled mode formalism of Section 2-3.



## 2.2 Modes of an Optical Fiber

An optical fiber is a cylindrical dielectric waveguide. It consists of a doped silica core surrounded by a pure silica cladding. Since the index of the core is greater than the index of the cladding, guiding is achieved via total internal reflection at the core/cladding interface.

To calculate the modes of the fiber, the wave equation is solved in cylindrical coordinates to accommodate the geometry of the fiber. Due to the complexity of the solutions for this case, it is easier to solve for the longitudinal field components first and then use Maxwell's equations to find the remaining transverse components. Following the treatment given by Pollock<sup>2</sup>, we begin with the scalar wave equation for the longitudinal field component  $E_z$ ,

$$\frac{1}{r} \frac{\partial}{\partial r} \left( r \frac{\partial E_z}{\partial r} \right) + \frac{1}{r^2} \frac{\partial^2 E_z}{\partial \phi^2} + \frac{\partial^2 E_z}{\partial z^2} + k_0^2 n^2 E_z = 0 \quad 2-11$$

where  $r$  is distance along the fiber radius,  $\phi$  is the azimuthal angle, and  $z$  is the distance along the fiber axis (Fig. 2-2).

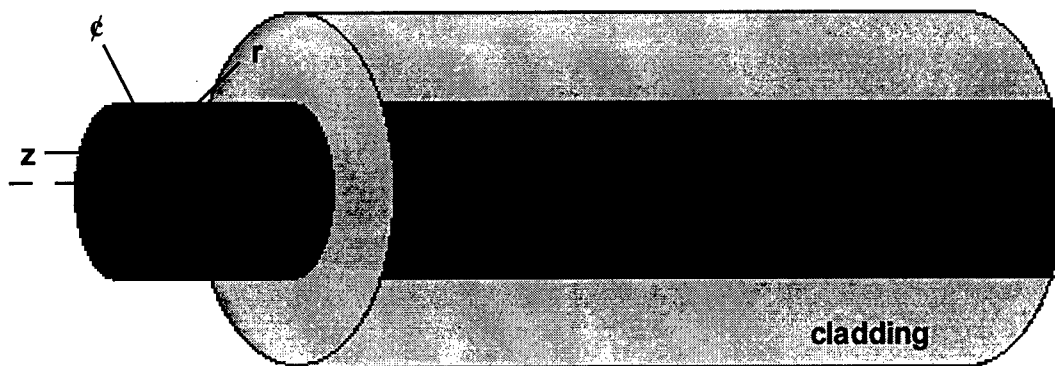


**Figure 2-2** Optical fiber waveguide consisting of a circular core surrounded by a lower index cladding.

$E_z$  is defined as an independent function of  $r$ ,  $\phi$ , and  $z$ , respectively, so that the technique of separation of variable may be employed,

$$E(r, \phi, z) = R(r)\Phi(\phi)e^{-i\beta z} \quad 2-12$$

where the  $e^{i\omega t}$  time dependence of the wave has been omitted for clarity, but is understood.

Substituting Eqn. 2-12 into Eqn. 2-11 yields,

$$\frac{1}{r} R' \Phi e^{-i\beta z} + R'' \Phi e^{-i\beta z} + \frac{1}{r^2} R \Phi'' e^{-i\beta z} - \beta^2 R \Phi e^{-i\beta z} + k_o^2 n^2 R \Phi e^{-i\beta z} = 0. \quad 2-13$$

Multiplying Eqn. 2-13 by  $r^2 / R \Phi e^{-i\beta z}$  and grouping like terms results in,

$$r^2 \frac{R''}{R} + r \frac{R'}{R} - r^2 \beta^2 + k_o^2 n^2 r^2 = -\frac{\Phi''}{\Phi}. \quad 2-14$$

The left-hand side of Eqn. 2-14 depends only on  $R$  while the right side depends only on  $\Phi$ .

By definition,  $R$  and  $\Phi$  vary independently. Thus both sides of this equation can be set equal to a separation constant  $v^2$ :

$$\Phi'' + v^2 \Phi = 0, \quad 2-15$$

and

$$r^2 \frac{\partial^2 R}{\partial r^2} + r \frac{\partial R}{\partial r} + r^2 (k_o^2 n^2 - \beta^2 - \frac{v^2}{r^2}) R = 0. \quad 2-16$$

The solution to the differential Eqn. 2-15 is [2],

$$\Phi(\phi) = \begin{cases} \cos(v\phi) \\ \sin(v\phi) \end{cases}. \quad 2-17$$

Given that the fiber is circularly symmetric,  $v$  must be an integer to satisfy the geometrical constraints of the problem.

Eqn. 2-16 is the differential equation for the Bessel functions. Its solutions are of the form,<sup>3</sup>

$$E_z(r, \varphi, z) = \begin{cases} AJ_v(\kappa r) e^{iv\varphi} e^{-i\beta z} + c.c. & r \leq a \\ CK_v(\gamma r) e^{iv\varphi} e^{-i\beta z} + c.c. & r \geq a \end{cases} \quad 2-18$$

where  $J_v$  is the Bessel function of the first kind of order  $v$ , and  $K_v$  is the Bessel function of the second kind of order  $v$ .  $\kappa$  is the transverse wavevector defined as,

$$\kappa = \sqrt{k_o^2 n^2 - \beta^2}, \quad 2-19$$

and  $\gamma$  is the attenuation coefficient defined as,

$$\gamma = \sqrt{\beta^2 - k_o^2 n^2}. \quad 2-20$$

In a similar fashion, the wave equation can also be solved for  $H_z$  resulting in [2],

$$H_z(r, \varphi, z) = \begin{cases} BJ_v(\kappa r) e^{iv\varphi} e^{-i\beta z} + c.c. & r \leq a \\ DK_v(\gamma r) e^{iv\varphi} e^{-i\beta z} + c.c. & r \geq a \end{cases} \quad 2-21$$

The transverse field components can now be determined by substituting the longitudinal field solutions into Faraday's law to generate  $E_r$ ,  $E_\varphi$ ,  $H_r$ , and  $H_\varphi$ :

$$E_r = \frac{-i}{\kappa^2} \left( \beta \frac{\partial E_z}{\partial r} + \frac{\omega \mu}{r} \frac{\partial H_z}{\partial \varphi} \right) \quad 2-22$$

$$E_\varphi = \frac{-i}{\kappa^2} \left( \frac{\beta}{r} \frac{\partial E_z}{\partial \varphi} - \omega \mu \frac{\partial H_z}{\partial r} \right) \quad 2-23$$

$$H_r = \frac{-i}{\kappa^2} \left( \beta \frac{\partial H_z}{\partial r} - \frac{\omega \varepsilon}{r} \frac{\partial E_z}{\partial \varphi} \right) \quad 2-24$$

$$H_\varphi = \frac{-i}{\kappa^2} \left( \frac{\beta}{r} \frac{\partial H_z}{\partial \varphi} + \omega \varepsilon \frac{\partial E_z}{\partial r} \right) \quad 2-25$$

To solve for the guided modes in the core ( $r \leq a$ ),  $E_z$  and  $H_z$  from Eqns. 2-18 and 2-21 are substituted into Eqns. 2-22 through 2-25. This results in four linear equations. In matrix form they are [2]:

$$\begin{bmatrix} J_v(\kappa a) & 0 & -K_v(\gamma a) & 0 \\ 0 & J_v(\kappa a) & 0 & -K_v(\gamma a) \\ \frac{\beta v}{a\kappa^2} J_v(\kappa a) & \frac{i\omega\mu}{\kappa} J_v'(\kappa a) & \frac{\beta v}{a\gamma^2} K_v(\gamma a) & \frac{i\omega\mu}{\gamma} K_v'(\gamma a) \\ -\frac{i\omega\epsilon_{core}}{\kappa} J_v'(\kappa a) & \frac{\beta v}{a\kappa^2} J_v(\kappa a) & -\frac{i\omega\epsilon_{clad}}{\gamma} K_v'(\gamma a) & \frac{\beta v}{a\gamma^2} K_v(\gamma a) \end{bmatrix} \begin{bmatrix} A \\ B \\ C \\ D \end{bmatrix} = 0. \quad 2-26$$

For non-trivial solutions, the determinate of this matrix must be equal to zero. Calculation of the determinant yields the dispersion relation, or characteristic equation of the fiber,

$$\frac{\beta^2 v^2}{a^2} \left[ \frac{1}{\gamma^2} + \frac{1}{\kappa^2} \right]^2 = \left[ \frac{J_v'(\kappa a)}{\kappa J_v(\kappa a)} + \frac{K_v'(\gamma a)}{\gamma K_v(\gamma a)} \right] \left[ \frac{k_o^2 n_{core}^2 J_v'(\kappa a)}{\kappa J_v(\kappa a)} + \frac{k_o^2 n_{clad}^2 K_v'(\gamma a)}{\gamma K_v(\gamma a)} \right]. \quad 2-27$$

This transcendental equation defines the allowed eigenvalues,  $\beta$ , for each mode. The possible mode solutions for a fiber are labeled as  $HE_{vm}$ ,  $EH_{vm}$ ,  $TE_{0m}$ , or  $TM_{0m}$ . Each mode corresponds to a discrete value of  $\beta_{vm}$  found from Eqn. 2-27. The mode label indices  $v$  and  $m$  are associated with the transverse variables  $r$  and  $\phi$ , respectively, and are thus integers. The label  $v$  is defined as the angular mode number and  $m$  as the radial mode number.

For the special case of  $v=0$ , the eigenvalue equation can be simplified. Only TE ( $E_z=0$ ) or TM ( $H_z=0$ ) modes exist in the fiber for this case. Because they are rotational invariant

( $\frac{\partial}{\partial \phi} = 0$ ) these modes propagate as meridional rays down the fiber. When  $v$  does not equal

zero the solutions to Eqn. 2-27 are the hybrid EH or HE modes. Hybrid modes consist of all six field components and thus have longitudinal field components for both  $\mathbf{E}$  and  $\mathbf{H}$ . The EH

or HE designation is dependent upon which longitudinal component,  $E_z$  or  $H_z$ , provides the largest contribution to the mode. Hybrid modes propagate as skew rays in the fiber and are rotationally invariant. In terms of the nomenclature, the lowest order mode, or fundamental mode, of a single mode fiber is the  $HE_{11}$  mode. This is followed by the  $TE_{01}$ ,  $TM_{01}$ , and  $HE_{21}$  modes. As discussed below, the alternative LP mode representation is often used in place of this designation because it is easier to calculate and experimentally observe.

### 2.2.1 LP Fiber Modes

Eqn. 2-27 can be difficult to evaluate, especially for large values of  $v$ . If it is assumed however that  $n_{\text{clad}}$  is approximately equal to  $n_{\text{core}}$ , Eqn. 2-27 becomes greatly simplified. This approach, used by Gloge<sup>4</sup> in his weakly guiding approximation, significantly eases computation but still yields accurate results since the core/cladding index difference of most fibers is typically very small.

Making the weakly guiding approximation in Eqn. 2-27 and rearranging terms by utilizing Bessel function identities yields [2],

$$\kappa \frac{J_{j-1}(\kappa a)}{J_{j-1}(\kappa a)} = -\gamma \frac{K_{j-1}(\gamma a)}{K_j(\gamma a)} \quad 2-28$$

where the subscript  $j$  is defined in terms of mode number  $v$ :

$j=1$	TE, TM modes
$j=v+1$	$EH_v$ modes
$j=v-1$	$HE_v$ modes

The basic premise behind this approximation is that in a weakly guiding fiber, linearly polarized light coupled into a fiber will remain linearly polarized. Polarized modes are obtained mathematically by superimposing certain combinations of hybrid modes. Because the resultant superposition modes are polarized in only one transverse direction ( $E_x$  or  $E_y$ ), they are called linear polarized or  $LP_{jm}$  modes. These modes are degenerate in  $v$  and  $\phi$  and are a superposition of degenerate  $EH_{v+1,m}$  and  $HE_{v-1,m}$  modes and degenerate  $TE_{om}$  and  $TM_{om}$  modes.

The lowest order mode, the  $LP_{01}$  mode, corresponds to the hybrid  $HE_{11}$  mode and is the fundamental mode in single mode fibers. It possesses a two-fold degeneracy which stems from the  $n_{\text{clad}}=n_{\text{core}}$  approximation. This degeneracy manifests itself as two orthogonally polarized  $LP_{01}$  modes ( $E_x$  or  $E_y$ ). The next order mode,  $LP_{11}$ , is a superposition of the  $TE_{01}$ ,  $TM_{01}$ , and  $HE_{21}$  modes. This and all other higher order LP modes have a four-fold degeneracy: two modes which are orthogonally polarized due to the  $n_{\text{clad}}=n_{\text{core}}$  approximation as above, and two which are caused by a  $\pm\phi$  dependency in the solutions. Calculated intensity plots of the  $LP_{01}$  and the  $LP_{11}$  are provided in Fig. 2-3.

In general, the intensity profile of a mode can be deduced from the mode subscripts  $j$  and  $m$ . The subscript  $j$  is one half the number of minima (or maxima) in the intensity distribution as a function of  $\phi$  from 0 to  $2\pi$ . Similarly, the subscript  $m$  is the number of maxima in the pattern that occurs on a radial line from zero to infinity.<sup>5</sup>

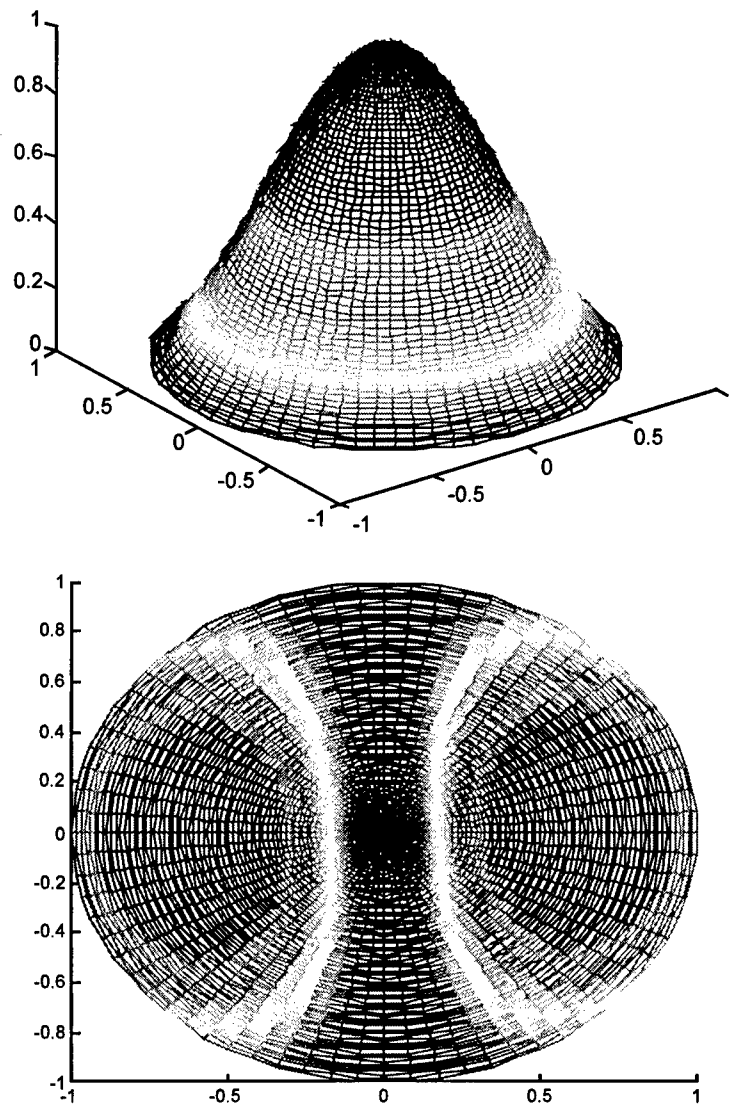


**Figure 2- 3** Calculated intensity plot of a  $LP_{01}$  fiber mode (top) and two dimensional cross section of a calculated  $LP_{11}$  fiber mode (bottom).

## 2.3 Fiber Grating Calculations

The basic waveguide and fiber concepts presented above are now used to calculate the spectral performance of fiber Bragg gratings. Central to the approach is the coupled mode theory. The basic coupled mode equations are derived in Section 2.3.1 using the formalism developed by Yariv.<sup>6</sup> In Section 2.3.2 these results are applied to the uniform grating problem. An extended coupled mode formalism is used in Section 2.3.3 for the case of non-uniform gratings. Finally in Section 2.3.4, tilted fiber gratings are discussed.

### 2.3.1 Coupled Mode Equations

As established in Section 2-1, waveguide modes are orthogonal and propagate independently of each other. In an ideal waveguide this is true as long as the dielectric constant of the guiding region remains uniform in the direction of propagation. In a reality, modes can transfer power and interact with each other due to deviations from ideal conditions in the waveguide. These deviations may be unintentional, as is the case for fabrication errors or bend losses, or they can be intentionally caused, as is the case for photo-induced fiber Bragg gratings.

To calculate mode coupling, deviations in the waveguide are modeled as a small perturbation of the dielectric constant which is periodic in the z-direction,  $\Delta\epsilon(x,y,z)$ . The dielectric constant is then written as

$$\epsilon(x,y,z) = \epsilon_o(x,y) + \Delta\epsilon(x,y,z), \quad 2-29$$

where  $\epsilon_o(x,y)$  is the ideal or unperturbed part.



In the ideal waveguide, the normal modes satisfy the wave equation for the unperturbed medium,

$$(\nabla^2 + k^2)\mathbf{E}(x, y) = 0, \quad 2-30$$

or by substituting in Eqn. 2-7,

$$\left[ \frac{\partial^2}{\partial x^2} + \frac{\partial^2}{\partial y^2} + \omega^2 \mu \epsilon(x, y) - \beta_m^2 \right] \mathbf{E}_m(x, y) = 0. \quad 2-31$$

In the perturbed waveguide, on the other hand,  $\Delta \epsilon(x, y, z)$  can couple energy from a given mode into other modes. As discussed in Section 2-1, the resulting field in the perturbed waveguide can be written as an expansion of the orthogonal modes of the unperturbed system,

$$\mathbf{E} = \sum_m A_m(z) \mathbf{E}_m(x, y) e^{-i\beta_m z}. \quad 2-32$$

Substituting Eqn. 2-32 and Eqn. 2.29 into the wave equation (Eqn. 2-30) yields,

$$\sum_m \left[ \frac{\partial^2 A_m}{\partial x^2} + \frac{\partial^2 A_m}{\partial y^2} + \frac{\partial^2 A_m}{\partial z^2} - i2\beta_m \frac{\partial A_m}{\partial z} - \beta_m^2 A_m \right] \mathbf{E}_m(x, y) e^{-i\beta_m z} = 0. \quad 2-33$$

The derivatives of  $\mathbf{E}$  with respect to  $x$  and  $y$  can be eliminated by use of Eqn. 2-31. Grouping the remaining derivatives on one side of the equation and rewriting the summations in terms of integers  $k$  and  $l$  (which can only assume values of  $m$ ) yields,

$$\sum_k \left[ \frac{\partial^2 A_k}{\partial z^2} - i2\beta_k \frac{\partial A_k}{\partial z} \right] \mathbf{E}_k(x, y) e^{-i\beta_k z} = -\omega^2 \mu \sum_l \Delta \epsilon(x, y, z) A_l \mathbf{E}_l(x, y) e^{-i\beta_l z}. \quad 2-34$$

Assuming that the perturbation is small, any mode coupling that occurs will be slowly varying and thus the parabolic approximation can be made. This assumes the second derivative terms are much smaller than the first derivative terms and may therefore be neglected,

$$\sum_k \left[ -i2\beta_k \frac{\partial A_k}{\partial z} \right] \mathbf{E}_k(x, y) e^{-i\beta_k z} = -\omega^2 \mu \sum_l \Delta \varepsilon(x, y, z) A_l \mathbf{E}_l(x, y) e^{-i\beta_l z}. \quad 2-35$$

Both sides of Eqn. 2-35 may be multiplied by  $\mathbf{E}_k^*$  and integrated over x and y,

$$\begin{aligned} (-i2\beta_k \frac{\partial A_k}{\partial z}) \iint \mathbf{E}_k(x, y) \cdot \mathbf{E}_k^*(x, y) dx dy = \\ -\omega^2 \mu \sum_l A_l \iint \mathbf{E}_k^*(x, y) \Delta \varepsilon(x, y, z) \mathbf{E}_l(x, y) e^{i(\beta_k - \beta_l)z} dx dy. \end{aligned} \quad 2-36$$

This allows the mode orthogonality relationship to be used. From Eqn. 2-9 this becomes

$$\frac{\partial A_k}{\partial z} = -\frac{\omega \beta_k}{4|\beta_k|} \sum_l A_l \iint \mathbf{E}_k^*(x, y) \Delta \varepsilon(x, y, z) \mathbf{E}_l(x, y) e^{i(\beta_k - \beta_l)z} dx dy. \quad 2-37$$

Eqn. 2-37 can be written in terms of a coupling coefficient,  $C_{kl}$

$$\frac{\partial A_k}{\partial z} = -i \frac{\beta_k}{|\beta_k|} \sum_l \sum_m A_l C_{kl} e^{i(\beta_k - \beta_l)z} \quad 2-38$$

where  $C_{kl}$  is defined as

$$C_{kl} = \frac{\omega}{4} \iint \mathbf{E}_k^*(x, y) \Delta \varepsilon(x, y, z) \mathbf{E}_l(x, y) dx dy. \quad 2-39$$

The coupling coefficient is an overlap integral whose magnitude describes how well a mode k couples to a mode l due to the perturbation  $\Delta \varepsilon(x, y, z)$ . If the perturbation  $\Delta \varepsilon(x, y, z)$  is zero, the coupling coefficient vanishes and no mode coupling occurs. If  $\Delta \varepsilon(x, y, z)$  is an even function, mode coupling can only occur between modes of the same parity (i.e. a forward propagating  $LP_{01}^+$  mode coupled to a backward propagating  $LP_{01}^-$  mode). On the other hand, when  $\Delta \varepsilon(x, y, z)$  is an odd function, mode coupling can only occur between different modes (i.e.  $LP_{01}^+ \rightarrow LP_{11}^-$ ). This is analogous to the interaction matrix element in quantum mechanical perturbation theory.<sup>7</sup>

Eqn. 2-38 represents an infinite set of coupled linear differential equations. In many practical problems, only two modes are significantly coupled. For two mode coupling problems, the modes will either be both traveling in the same direction (co-directional coupling) or they will be traveling in opposite directions (contra-directional coupling). It is the latter case which is of interest since it represents the situation for a reflection fiber Bragg grating. Labeling the two modes mode 1 and mode 2 and assuming mode 1 is the incident wave and mode 2 is the reflected wave,

$$\beta_1 = \frac{2\pi n_{eff}}{\lambda} = -\beta_2, \quad 2-40$$

Where  $n_{eff}$  is the effective mode index. Eqn. 2-38 then reduces to two linearly coupled differential equations,

$$\frac{\partial A_1}{\partial z} = -iC_{12}A_2e^{i2\beta z} \quad 2-41$$

$$\frac{\partial A_2}{\partial z} = iC_{21}A_1e^{-i2\beta z} \quad 2-42$$

where  $\beta_1 = -\beta_2 = \beta$

### 2.3.2 Uniform Fiber Bragg Grating

A uniform grating is defined as having a sinusoidal index modulation with a constant or uniform average index (Fig. 2-4). For this model it will be assumed that the uniform fiber Bragg grating is written in a single mode fiber, is untilted, and is a reflection grating. In this case the grating will couple a forward propagating  $LP_{01}^+$  mode into a backward propagating  $LP_{01}^-$  mode. A grating of this type may be modeled with a sinusoidal index perturbation in the fiber core given by,

$$n_{eff}(z) = n_{core} + n_1 \cos\left(\frac{2\pi}{\Lambda} z\right) \quad 2-43$$

where  $\Lambda$  is the period of the grating and  $n_1$  is the magnitude of the index.

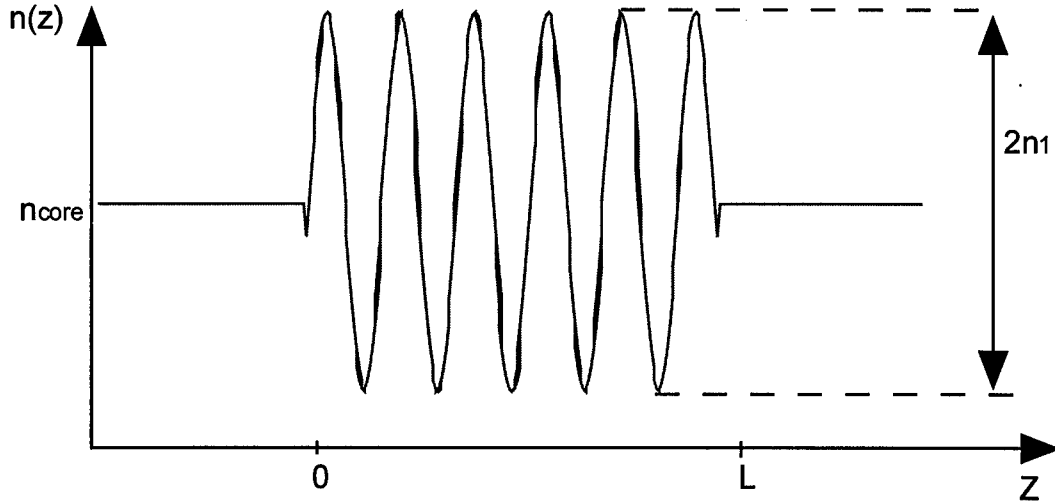


**Figure 2- 4** Sinusoidal index profile (Eqn. 2-43) for a uniform fiber grating. The average index is uniform. The grating has a length  $L$ .

The first step in modeling a grating is to calculate the coupling coefficient, for which

$\Delta\epsilon(x, y, z)$  is needed. From Eqn. 2-29,

$$\Delta\epsilon(x, y, z) = \epsilon(x, y, z) - \epsilon_o(x, y), \quad 2-44$$

where,

$$\epsilon(x, y) = \epsilon_o n^2(x, y). \quad 2-45$$

Applying Eqn. 2-43,

$$\epsilon(x, y, z) = \left[ n_{core}^2 + 2n_{core}n_1 \cos\left(\frac{2\pi}{\Lambda} z\right) + n_1^2 \cos^2\left(\frac{2\pi}{\Lambda} z\right) \right] \epsilon_o \quad 2-46$$

where  $n_{core}$  is the index of the fiber core and  $n_1$  is the index modulation as illustrated in Fig. 2-

4. Assuming a small index modulation ( $n_1 \ll 1$ ), the last term of Eqn. 2-46 will be very small and can be ignored.  $\Delta \varepsilon(x, y, z)$  is then approximated by,

$$\Delta \varepsilon(x, y, z) = 2n_{core}n_1 \cos\left(\frac{2\pi}{\Lambda}z\right)\varepsilon_o \quad 2-47$$

By substituting this into Eqn. 2-39 and converting to cylindrical coordinates, the coupling coefficient becomes,

$$C_{01^+01^-} = \frac{\omega}{2}n_{core}n_1 \cos\left(\frac{2\pi}{\Lambda}z\right)\varepsilon_o \int_0^{2\pi} \int_0^a E_{LP_{01^+}}^*(r, \vartheta) E_{LP_{01^-}}(r, \vartheta) r dr d\vartheta, \quad 2-48$$

where the subscripts indicate coupling between forward and backward traveling  $LP_{01}$  modes.

Notice that the integral on the right side of the equation is similar in form to the Poynting equation. Since the integration is performed over the core, it represents the total amount of energy propagating in the core of the fiber. This is known as the core power confinement factor,  $\Gamma$ .

The coupling coefficient is usually written in reduced form as,

$$C_{01^+01^-} = 2\kappa \cos\left(\frac{2\pi}{\Lambda}z\right) = C_{01^+01^-}^*, \quad 2-49$$

where  $\kappa$  is defined as the coupling constant

$$\kappa = \frac{\pi n_1 \Gamma}{\lambda}. \quad 2-50$$

The coupled mode equations then take the form,

$$\frac{\partial A_1}{\partial z} = -i\kappa A_2 \left( e^{i[\frac{2\pi}{\Lambda} + 2\beta]z} + e^{-i[\frac{2\pi}{\Lambda} - 2\beta]z} \right) \quad 2-51$$

$$\frac{\partial A_2}{\partial z} = i\kappa A_1 (e^{i[\frac{2\pi}{\Lambda} - 2\beta]z} + e^{-i[\frac{2\pi}{\Lambda} + 2\beta]z}) \quad 2-52$$

The first term in the parentheses of both equations is a positive exponential that is rapidly oscillating, and hence has a negligible contribution.<sup>8</sup> The second term in the parentheses represents the phase mismatch between the two modes. The grating term in this exponential can compensate for the mode mismatch when the Bragg condition is satisfied. Eliminating the first phase term yields,

$$\frac{\partial A_1}{\partial z} = -i\kappa A_2 e^{i2\delta z} \quad 2-53$$

$$\frac{\partial A_2}{\partial z} = i\kappa A_1 e^{-i2\delta z} \quad 2-54$$

where  $\lambda_B$  is the Bragg wavelength of the grating,  $\lambda$  is the wavelength of operation,  $\Lambda = \frac{\lambda_B}{2n}$

is the grating period, and  $\delta$  is defined as the Bragg detuning parameter,

$$\delta = \frac{1}{2} \left( 2\beta - \frac{2\pi}{\Lambda} \right) = 2\pi n \left[ \frac{1}{\lambda} - \frac{1}{\lambda_B} \right] \quad 2-55$$

$\delta$  is a measure of the Bragg, or phase, mismatch between the modes. When the Bragg condition is met,  $\delta$  is equal to zero and resonant mode coupling occurs. As  $\delta$  increases, i.e. larger Bragg mismatching, mode coupling decreases to zero.

As is indicated Fig. 2-4, the grating is defined as having a length  $L$  that extends from  $z=0$  to  $z=L$ . If we assume that the forward propagating wave is incident at the start of the grating (let  $A_1(0)=1$ ) and there is no energy in the reflected wave at the end of the grating ( $A_2(L)=0$ ), then

a closed form solution subject to these boundary conditions can be found for Eqns. 2-53 and

2-54. The closed form solution gives the reflected power  $R = \left| \frac{A_2(0)}{A_1(0)} \right|^2$ ,

$$R = \frac{(\kappa L)^2 \sinh^2(\sqrt{(\kappa L)^2 - (\delta L)^2})}{(\kappa L)^2 \cosh^2(\sqrt{(\kappa L)^2 - (\delta L)^2}) - (\delta L)^2} \quad 2-56$$

Several important grating properties can be calculated from Eqn. 2-56.<sup>10</sup> For example, Fig. 2-5 illustrates how grating reflectivity changes as a function of the coupling constant. As the  $\kappa L$  product increases, the reflectivity increases, the grating bandwidth widens, and the strength of the sidelobes increases.

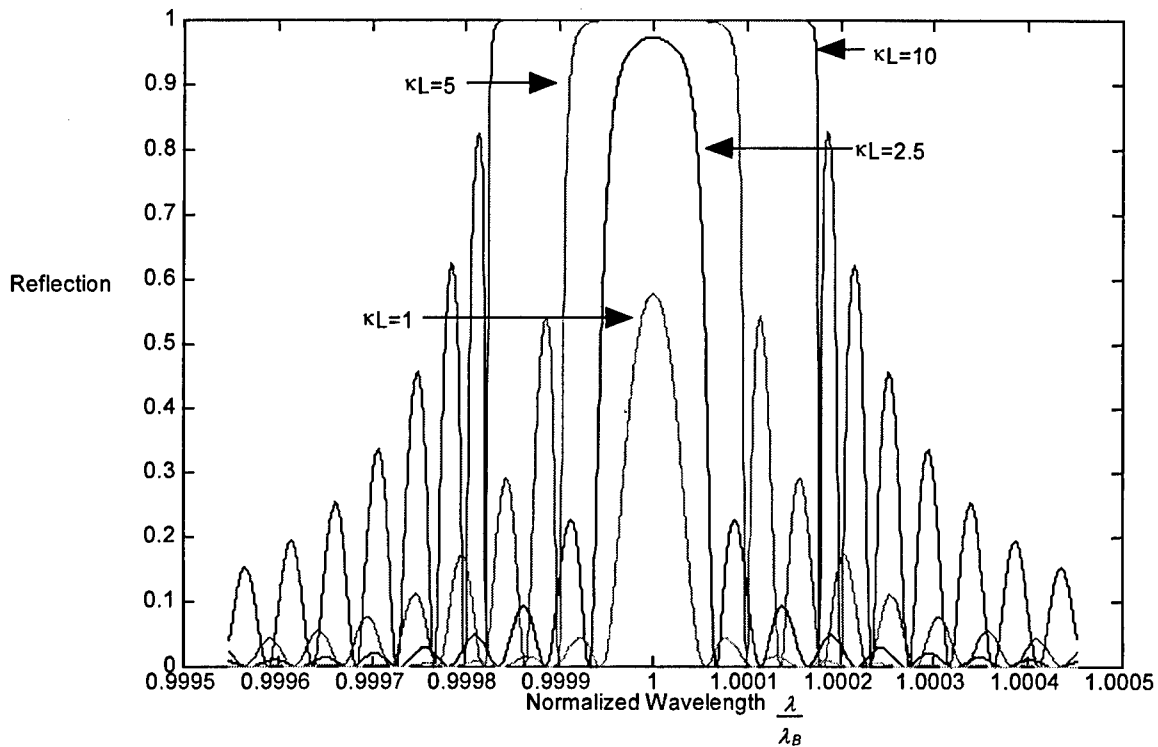


**Figure 2- 5** Reflection spectra of a uniform fiber grating as a function of  $\kappa L$

The bandwidth of the grating can be determined by manipulating the numerator of Eqn. 2-56.

Dividing the equation by  $(\kappa L)^2$ , and using the identity,

$$\sinh(ix) = i \sin(x), \quad 2-57$$

the numerator of Eqn. 2-56 becomes,

$$\sin(\sqrt{(\delta L)^2 - (\kappa L)^2}). \quad 2-58$$

The bandwidth of the grating is defined as the distance between the first zeros in the reflection spectrum on either side of the peak reflectivity. These zeros occur when the argument of Eqn.

2-58 equals  $\pi$  or,

$$\frac{\Delta \lambda_{zero}}{\lambda_B} = \frac{\Delta n}{n_0} \sqrt{1 + \left( \frac{\lambda_B}{\Delta n L} \right)^2} \quad 2-59$$

where the coupling constant from Eqn. 2-50 has been used with  $\Delta n = \Gamma n_1$ . There are two

important limits to Eqn. 2-59. The first occurs when  $\Delta n$  is small ( $\Delta n \ll \frac{\lambda_B}{L}$ ). The grating is

considered “weak” and in this limit Eqn. 2-59 approaches,

$$\frac{\Delta \lambda_{zero}}{\lambda_B} = \frac{\lambda_B}{n_0 L}. \quad 2-60$$

Thus in the weak grating case, the bandwidth is inversely proportional to length. This is a reasonable result since light will traverse more grating periods in a longer grating and have a narrower bandwidth reflection spectrum as a result of phase matching over a greater number of fringe planes. A plot of grating bandwidth versus coupling constant for a weak grating is given in Fig. 2-6. For this calculation  $\Delta n = 10^{-5}$  is fixed and the length  $L$  of the grating is

varied. The grating has a center Bragg wavelength of  $\lambda_B = 1550nm$  and satisfies  $\Delta n \ll \frac{\lambda_B}{L}$ .



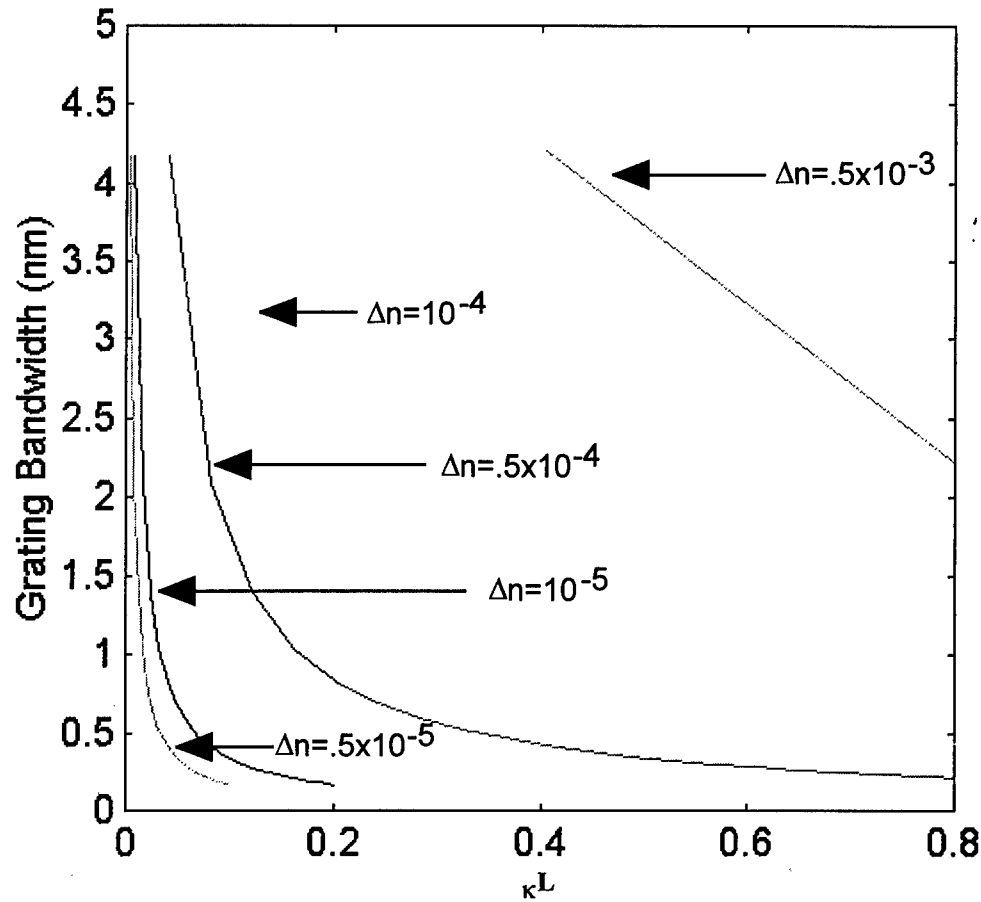


**Figure 2- 6** Calculation of grating bandwidth as a function of coupling constant for the case of a weak grating. The length  $L$  of the grating is varied for several cases of fixed  $\Delta n$ .

For the opposite limit,  $\Delta n \gg \frac{\lambda_B}{L}$ , the grating is considered “strong” and Eqn. 2.59

approaches,

$$\frac{\Delta\lambda_{\text{zero}}}{\lambda_B} = \frac{\Delta n}{n_0}. \quad 2-61$$

In this limit, the bandwidth becomes independent of grating length and depends only on the index modulation. Light propagating through a strong grating is mostly reflected before it reaches the end of the grating, thus negating the full effect of the grating length.

The bandwidth of a strong uniform grating as a function of the coupling constant is given in Fig. 2-7.  $\Delta n$  is varied for several cases of fixed length. Again  $\lambda_B = 1550\text{nm}$  and in this case

$$\Delta n \gg \frac{\lambda_B}{L}.$$

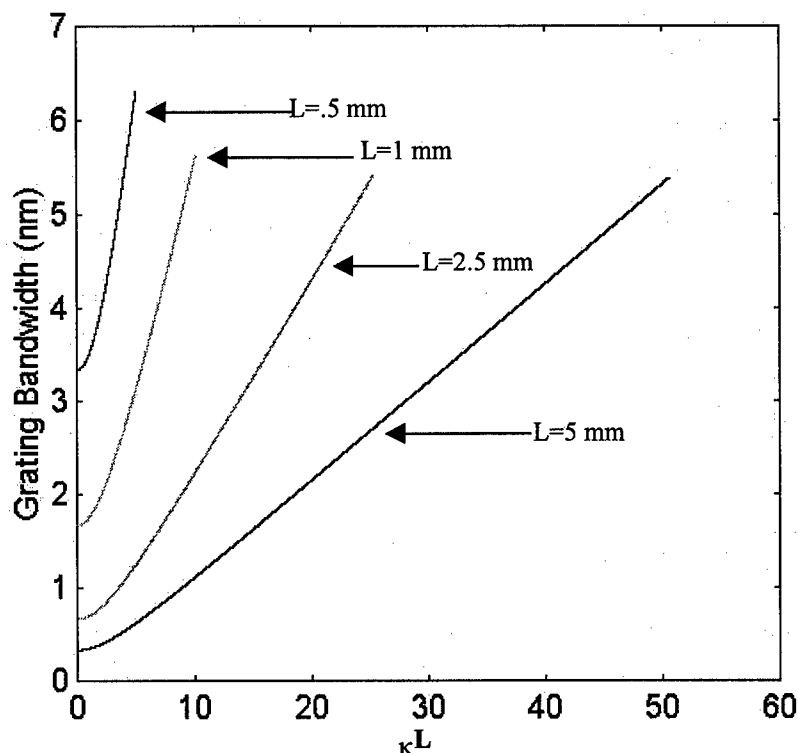


**Figure 2- 7** Calculation of grating bandwidth as a function of coupling constant ( $\Delta n$  is varied) for the case of a strong grating. Several cases of fixed length,  $L$ , are plotted.

Another important characteristic of a grating is its peak reflectivity. In general, maximum coupling occurs when  $\delta=0$  (or when  $\lambda=\lambda_B$ ). When resonance does occur, Eqn. 2-56 reduces to

$$R_{\max} = \tanh^2(\kappa L). \quad 2-62$$

In Fig. 2-8,  $R_{\max}$  is plotted as a function of the coupling constant. As shown in the figure saturation begins to occur for  $\kappa L \geq 4$ .

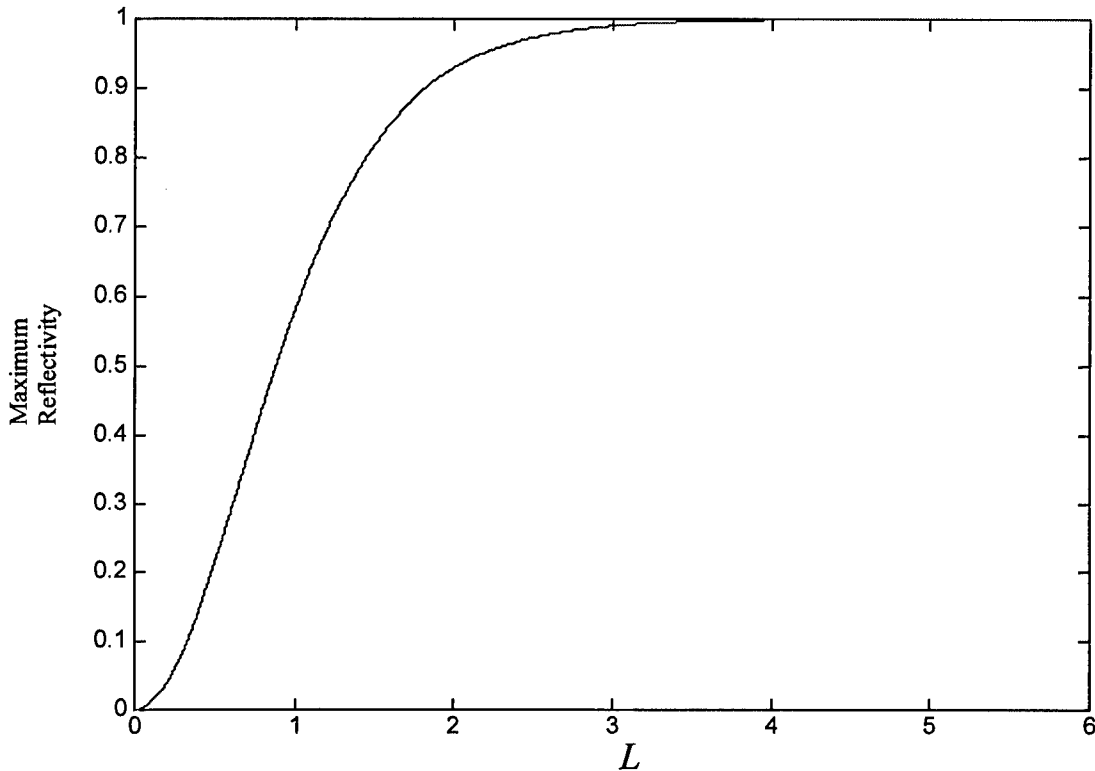


**Figure 2- 8** Calculation of maximum grating reflectivity as a function of coupling constant.

Eqn. 2-62 may be used to calculate  $\Delta n$  from experimental data if the grating length and reflectivity are known. This approach is used in Chapter 3 to compare these calculations with experimental results.

### 2.3.3 Non-uniform Gratings

The intensity profile of the laser beam used to write a fiber grating determines the index profile produced in the fiber. The index profile, in turn, determines the spectral characteristic

of the grating. The reflection spectrum of a grating can thus be tailored by apodizing the writing beams to create a non-uniform grating. As opposed to uniform gratings which typically have a reflection spectra with strong sidelobes (as was shown in Fig. 2-5), non-uniform index profile gratings can be created with the spectral characteristics required for a specific application.

Non-uniform gratings may be modeled by a raised cosine index modulation given by<sup>11</sup>

$$n(z) = n_{core} + n_1(z)(1 + \cos(\frac{2\pi}{\Lambda} z)) \quad 2-63$$

where  $n_1(z)$  is a spatially varying envelope function of the induced index perturbation.

Although many profiles are possible,  $n_1(z)$  will take the form of a Gaussian in this dissertation unless otherwise stated. For the gratings of interest, this is an accurate representation of the index profile since the gratings are formed with laser beams having a Gaussian profile. Thus  $n_1(z)$  is given by,<sup>12</sup>

$$n_1(z) = n_1 \exp(-4 \ln 2 \frac{z^2}{FWHM^2}). \quad 2-64$$

Fig. 2-9 is a representation of a Gaussian grating index profile. The center line in the figure represents the spaced average index across the grating. As a grating is written, this index will increase until saturation occurs.

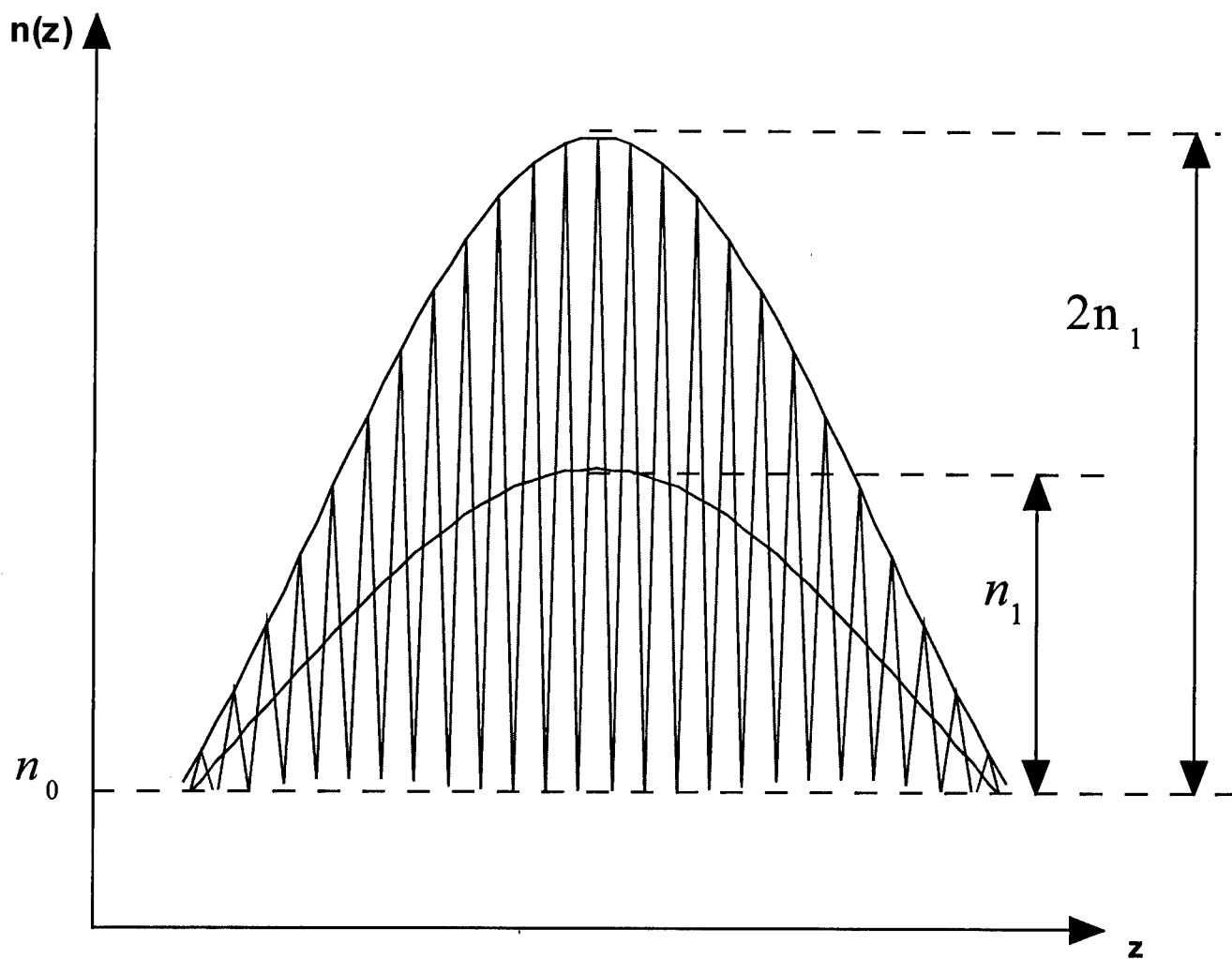


**Figure 2- 9** Non-uniform Gaussian index profile distribution. The center line represents the average index of the grating and  $2n_1$  is the peak-to-peak index modulation.

In the uniform grating model of Section 2.3.2, the average index remained independent of grating strength and the peak of the grating reflection remained centered at  $\lambda_B$ . In the non-uniform grating case the increase in the average index with exposure causes the grating spectrum to red shift in wavelength. Since the index change is larger in the center of the grating, this portion is red-shifted by a greater amount than the rest of the grating. As a result, it reflects light at a longer wavelength. The peak of the grating reflectivity (associated with the peak index) is thus shifted away from  $\lambda_B$ . The weaker parts of the grating, on the other hand, are not red shifted as much as the center of the grating and have their local resonances at shorter wavelengths. A shorter wavelength is transparent to the center of the grating and is not reflected by it. As a result, effective Fabry-Perot cavities with resonance peaks on the short wavelength side of the peak reflectivity are formed [11].

This situation can be analyzed using the extended coupled mode formalism of Erdogan and Sipe.<sup>13</sup> Bound-mode to bound-mode coupling in non-uniform gratings with either straight or tilted fringes may be calculated with this method. In this approach, the coupled mode equations become,

$$\frac{\partial u}{\partial z} = i\bar{\beta}[g_f\sigma(z) + \delta - \frac{1}{2\bar{\beta}}\frac{\partial\phi}{\partial z}]u(z) + i\bar{\beta}g_b\kappa(z)v(z) \quad 2-65$$

$$\frac{\partial v}{\partial z} = -i\bar{\beta}[g_f\sigma(z) + \delta - \frac{1}{2\bar{\beta}}\frac{\partial\phi}{\partial z}]v(z) - i\bar{\beta}g_b\kappa(z)u(z) \quad 2-66$$

Where  $u(z)$  and  $v(z)$  are the forward and backwards propagating waves in the fiber,  $\sigma(z)$  represents the slowly varying Gaussian background index,  $\kappa(z)$  is the amplitude of the index modulation,  $\phi$  represents the variation or chirp in the period of the grating, and  $g_f$  and

$g_b$  are the coupling coefficients for forward and backward scattering from the fiber grating, respectively.

Unlike the simpler case of the uniform grating, a closed form solution to Eqns. 2-65 and 2-66 is difficult. Therefore numerical analysis must be used. A program was written in MATLAB using an adaptive step size Runge-Kutta integration algorithm to accomplish this. Runge-Kutta is typically used for boundary value problems with initial conditions at a single point. For a reflection grating the initial conditions of  $u(0)=1$  (arbitrary) and  $v(L)=0$  are usually used for the forward traveling and reflected waves. Redefining this into the necessary format of a single point boundary value problem (as opposed to a two point problem), the initial boundary conditions of  $u(L)=1$  and  $v(L)=0$  were used and integration was then performed backwards

from  $z=L$  to  $z=0$ . The grating reflectivity is then calculated at  $z=0$  by  $R = \frac{|v(0)|^2}{|u(0)|^2}$ .

A constraint in performing this calculation was that the Runge-Kutta routine in MATLAB could not converge with equations written explicitly in terms of imaginary numbers. To overcome this problem, the equations were factored into real and imaginary parts and separated via the substitutions,

$$u \rightarrow u' + iu'' \quad 2-67$$

$$v \rightarrow v' + iv'' \quad 2-68$$

where a single prime denotes the real part and a double prime is the imaginary part. This produces four equations which are then solved simultaneously.

To verify this approach, the simpler uniform grating which has a closed form solution was used as a test case. The grating spectrum was calculated both numerically and with the closed form solution of Eqn. 2-56 and the results were compared. This was repeated for a variety of index modulations and grating lengths to ensure validity. An example of the results for the case of a 1 mm long grating with an index modulation of approximately  $\Delta n = 10^{-3}$  is shown in Fig. 2-10. In this case, as well as the others tested, the results of the numerical analysis matched those derived from the closed form solutions.

With the numerical technique proven to be accurate for the uniform case, it was used to calculate the solution to Eqns. 2-65 and 2-66. The results for the case of a straight grating with a Gaussian envelope of 5 mm (FWHM) and a Bragg wavelength of 1550 nm is shown in Fig. 2-11. The peak of the grating reflectivity is shifted from  $\lambda_B$  due to the non-uniform index distribution as described above. Also, there are resonances on the short wavelength side of the grating peak as expected. The number of Fabry-Perot resonances are a function of grating strength and increase with increased index modulation.

## 2.4 Summary

The tools used to model fiber Bragg grating characteristics were presented. Several different grating types were discussed. The techniques used to fabricate these grating types are discussed in Chapters 3.



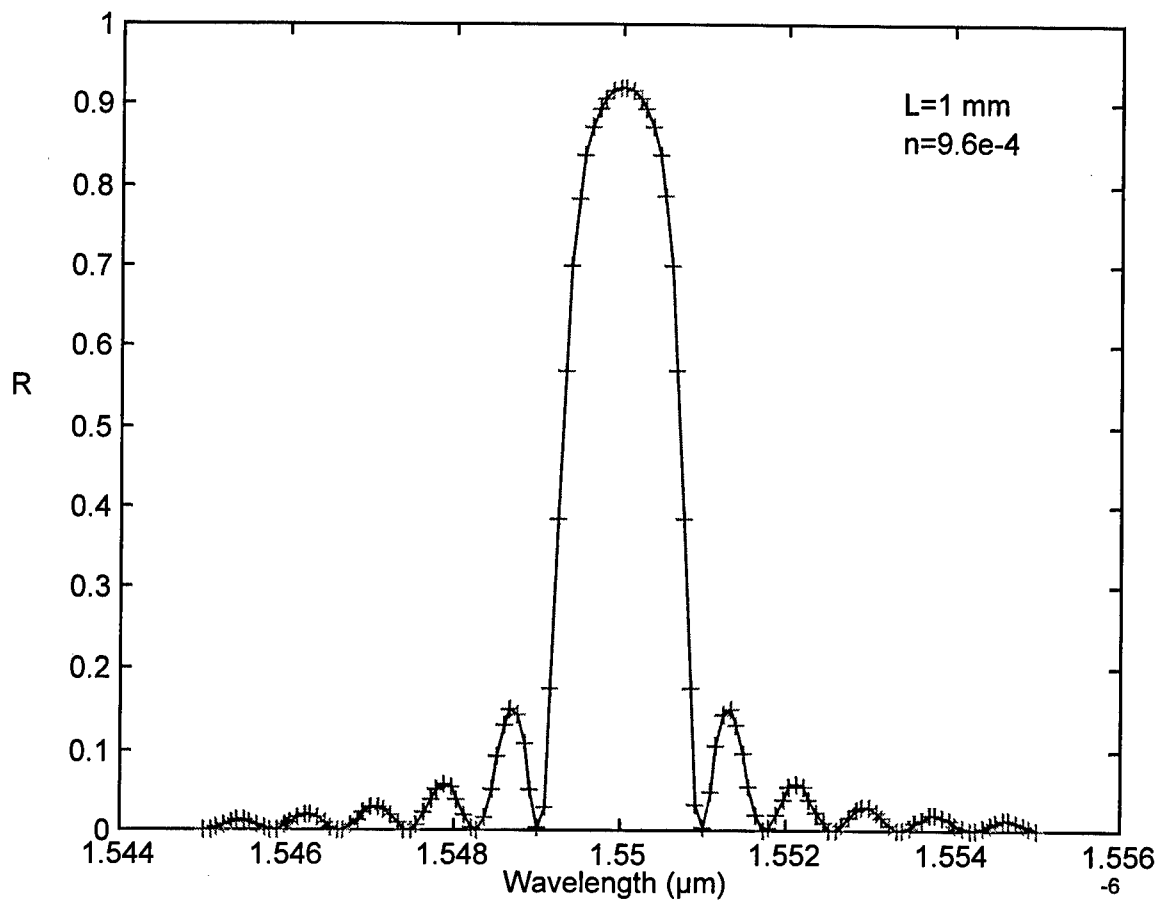


**Figure 2- 10** Reflection spectrum of a uniform grating calculated by both the closed form solution (solid line) and numerically (plus marks).

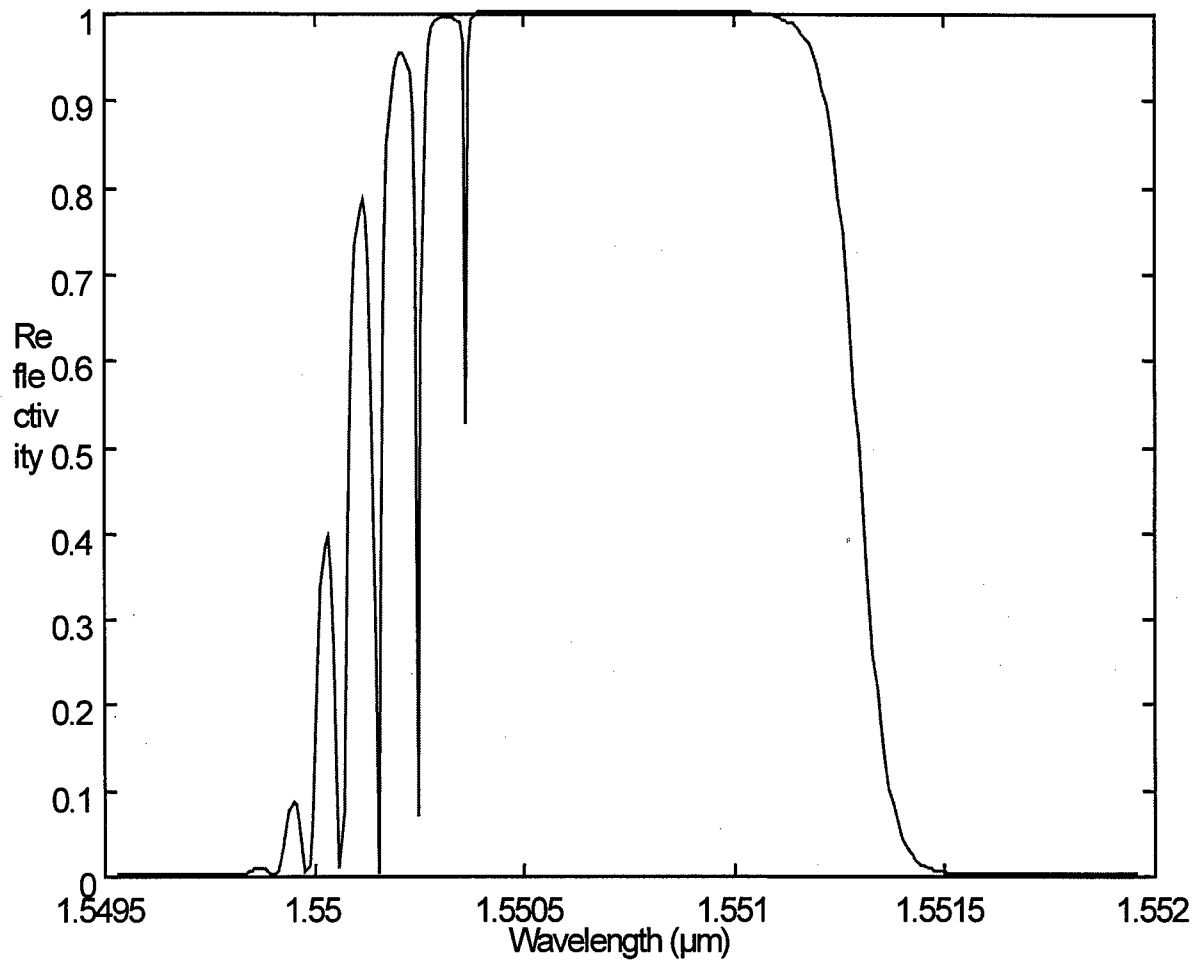


**Figure 2-11** Reflection spectrum of a fiber grating with a Gaussian index profile (5mm (FWHM),  $\lambda_B=1500\text{nm}$ ,  $n_{\text{clad}}=1.44$ ,  $\Delta=.0055$ ,  $\sigma=10^{-3}$ .)

- 
- <sup>1</sup> H. Kogelnik, "Theory of optical waveguides," in Guided-Wave Optics, T. Tamir, Ed. (Springer-Verlag, New York, 1990).
- <sup>2</sup> C. R. Pollock, Fundamentals of Optoelectronics, (Irwin, Chicago, 1995).
- <sup>3</sup> G. Arfken, Mathematical Methods For Physicists, Third Ed., (Academic Press Inc., Boston, 1985), p. 578.
- <sup>4</sup> D. Gloge, "Weakly Guiding Fibers," Appl. Opt., vol. 10, pp. 2252-2258, 1971.
- <sup>5</sup> J. A. Buck, Fundamentals of Optical Fibers, (John Wiley and Sons New York, 1995).
- <sup>6</sup> A. Yariv, and P. Yeh, Optical Waves in Crystals, (John Wiley and Sons New York, 1984).
- <sup>7</sup> N. Peyghambarian, S. W. Koch, A. Mysrowicz, Introduction to Semiconductor Optics, (Prentice Hall, Englewood Cliffs, New Jersey, 1993).
- <sup>8</sup> D. L. Lee, Electromagnetic Principles of Integrated Optics, (John Wiley and Sons New York, 1986).
- <sup>9</sup> A. Yariv, and P. Yeh, Optical Waves in Crystals, (John Wiley and Sons New York, 1984).
- <sup>10</sup> T. Erdogan, "Fiber Grating Spectra," J. Lightwave Technol., vol. 15, pp. 1277-1294, 1997.
- <sup>11</sup> V. Mizrahi, and J. E. Sipe, "Optical Properties of Fiber Phase Gratings," J. Lightwave Technol., vol. 11, pp. 1513-1517, 1993.
- <sup>12</sup> T. Erdogan, "Cladding-mode resonances in short- and long-period fiber grating filters," J. Opt. Soc. Am. A, vol. 14, pp. 1760-1773, 1997.
- <sup>13</sup> T. Erdogan, and J. E. Sipe, "Tilted fiber phase gratings," J. Opt. Soc. Am. A, vol. 13, pp. 296-312, 1996.

## **Chapter 3: Fiber Bragg Grating Formation**

In this chapter, the fundamental concepts behind the experimental fabrication of fiber Bragg gratings are presented. To describe the formation of fiber gratings, a review of the photoinduced mechanism responsible is first presented in Section 3.1. This photoinduced change in germania-silica fiber can also be enhanced with hydrogen gas. Section 3.2 discusses the important control parameters for hydrogen loading and describes a loading system designed and constructed to sensitize fibers. In Section 3.3, a general overview of grating writing techniques is given. The formation of unslanted, reflection fiber and the experimental setup used to fabricate them is presented in Section 3.4.

### **3.1 Photosensitivity in Optical Fibers**

Photosensitivity in optical fiber is defined as the change in the refractive index within the fiber due to laser exposure, usually in the UV. Although the details of the process are still not well understood, one popular model attributes photosensitivity to germanium related defects in the fiber core as described below.

Optical fiber is typically made of glass with a tetrahedral structure consisting of silicon and oxygen atoms. In this matrix, silicon has four valence electrons and oxygen has two. Thus each silicon atom is singly bonded to four oxygen atoms. The cladding of a fiber is composed of pure silica ( $\text{SiO}_2$ ) glass. The core of the fiber, on the other hand, is usually doped with germanium to increase its index of refraction (this allows total internal reflection to occur at the core/cladding interface). Germanium, like silicon, has four valence electrons and can

replace silicon in the glass structure. This substitution, however, produces defects when the germanium doesn't bond properly. The resulting defects are known as color centers and are believed to be the origin of the photosensitivity effect.

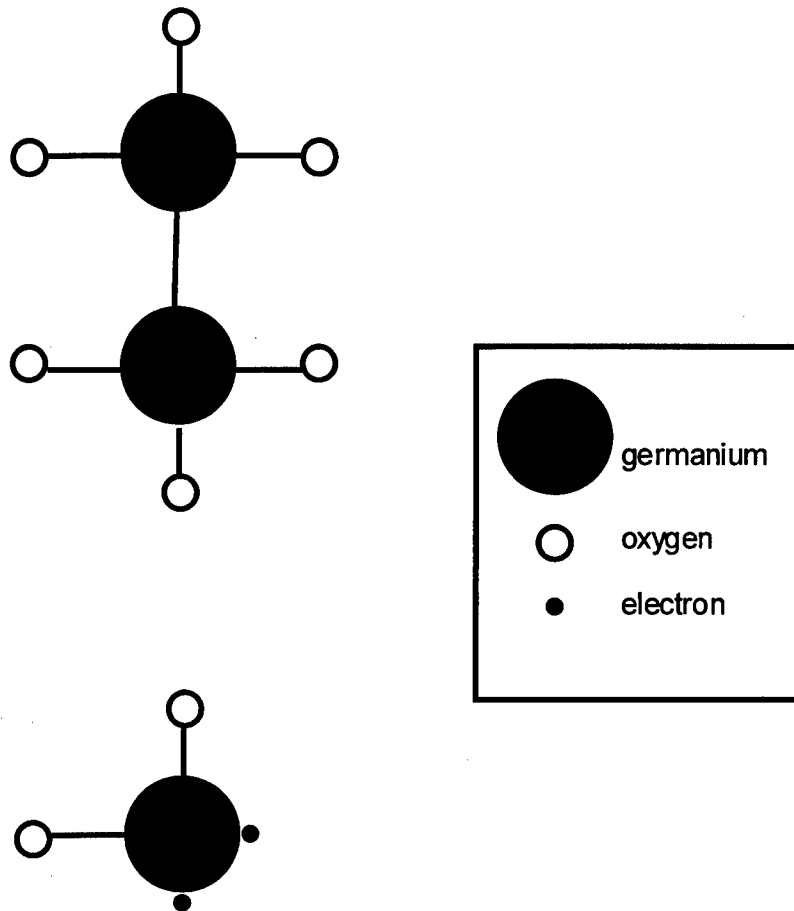
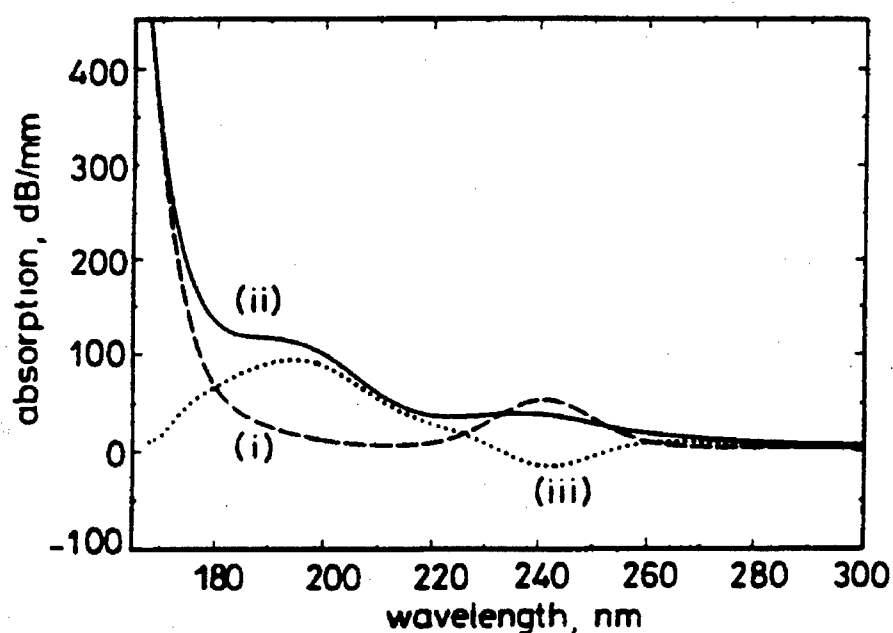


**Figure 3- 1** Basic GeO defect structures.

Two basic kinds of germanium oxygen deficient defects have been proposed. They are illustrated in Fig. 3-1. The first is shown at the top of the figure and is known as a neutral oxygen vacancy (NOV).<sup>1</sup> A NOV occurs when a germanium atom has a silicon or germanium atom as its nearest neighbor instead of an oxygen atom. The second defect at the bottom of

the figure arises when a germanium atom is bonded to only two oxygen atoms. This leaves the germanium atom with a lone pair of electrons which are unbonded.<sup>2</sup> An important difference between these defects is that the NOV defect can be bleached by irradiation in the 240 nm wavelength band. It is therefore commonly believed that the NOV defect is primarily responsible for photosensitivity, but the role of each type of defect and the interaction between them is still not well understood.



***UV spectra of 3 mol% germania MCVD core before and after UV exposure***

- (i) UV absorption of MCVD core prior to UV exposure**
- (ii) UV spectrum of MCVD core after 30 min UV exposure**
- (iii) UV spectral changes induced by 30 min UV exposure**

**Figure 3- 2** UV absorption spectrum of 3 % mole germanium doped fiber perform before and after UV exposure. Taken from [3].

Both defects do exhibit absorption in the 240 nm wavelength band. Fig. 3-2 is the measured UV absorption spectrum of a germanium doped fiber perform both before and after exposure to UV light at 248 nm.<sup>3</sup> The key point of the figure is that after UV exposure, there is a decrease in the absorption in the 240 nm band. This bleaching suggests that the defect responsible for the initial absorption has been eliminated.

One of the most popular models used to explain this phenomenon is the color center model.<sup>4</sup> In this hypothesis, it is believed that UV light ionizes the oxygen deficient color centers causing electrons to be released. The freed electrons are then trapped in neighboring sites, creating new types of color centers (i.e. Ge(1) and Ge(2)).<sup>5</sup> Hence while some defects are bleached, others are created and the net result is a local redistribution of electrons which modifies the UV absorption profile of the glass (Fig. 3-2). A change in absorption can then be related to a change in the index of refraction by the Kramers-Kronig relation,<sup>6</sup>

$$\Delta n(\omega') = \frac{c}{\pi} P \int \frac{\Delta \alpha(\omega) d\omega}{\omega^2 - \omega'^2}, \quad 3-1$$

where the P stands for the principal part of the integral and  $\Delta \alpha$  is the change in absorption. Thus a change in the absorption in the core of the fiber caused by exposure to an UV interference pattern can result in a nonvolatile modulation of the index of refraction in the core and can be used to form a grating in the fiber.

The magnitude of the induced refractive index change varies from fiber to fiber and is a function of germanium doping levels. This is logical since it is the germanium-related defects which are believed responsible for the effect. It has been shown that absorption, and thus

index change, depends linearly on germanium concentration up until the onset of saturation.<sup>7</sup>

Saturation is both a function of energy density and duration of exposure. For standard communication fiber which is doped with 3-6 mole % GeO<sub>2</sub>, the UV induced index change typically does not exceed 10<sup>-4</sup>.<sup>8</sup>

### 3.2 Hydrogen Loading

A technique developed to increase the photosensitivity of almost any germanosilicate fiber is "hydrogen loading."<sup>9</sup> High pressure loading of hydrogen gas into the fiber core causes nearly every germania site in the glass to participate in the formation of defects. This dramatically increases the magnitude of the refractive index change obtainable and allows strong gratings to be written in almost any standard telecommunications fiber. Index changes as high as 10<sup>-2</sup> have been reported.<sup>10</sup>

The amount of hydrogen which may be introduced into a fiber is a function of temperature, time, and pressure. The influence of these parameters on the diffusion rate of hydrogen into the core of a fiber can be modeled by using a Fickian diffusion equation. This models a circular cylinder in which diffusion is everywhere radial. To calculate hydrogen diffusion into the fiber core, the fiber is treated as a cylinder with a radius equal to the fiber cladding. The normalized concentration of hydrogen at the core of a fiber with radius  $a$  is then given by<sup>11</sup>

$$\frac{C}{C_0} = 1 - \frac{2}{a} \sum_{n=1}^{\infty} \frac{\exp(-D\alpha_n^2 t) J_0(r\alpha_n)}{\alpha_n J_1(a\alpha_n)} \quad 3-2$$



where  $D$  is the diffusion constant of hydrogen in silica,  $t$  is time,  $r$  is the radial distance from the center of the core, and  $r\alpha_n$  and  $a\alpha_n$  are the roots of the Bessel function of the first kind of orders zero and one, respectively. The diffusion constant,  $D$ , is temperature dependent and has been found empirically to be<sup>12</sup>

$$D = 2.83 \times 10^{-4} \exp(-4834/T) \text{ cm}^2/\text{sec}.$$

3- 3

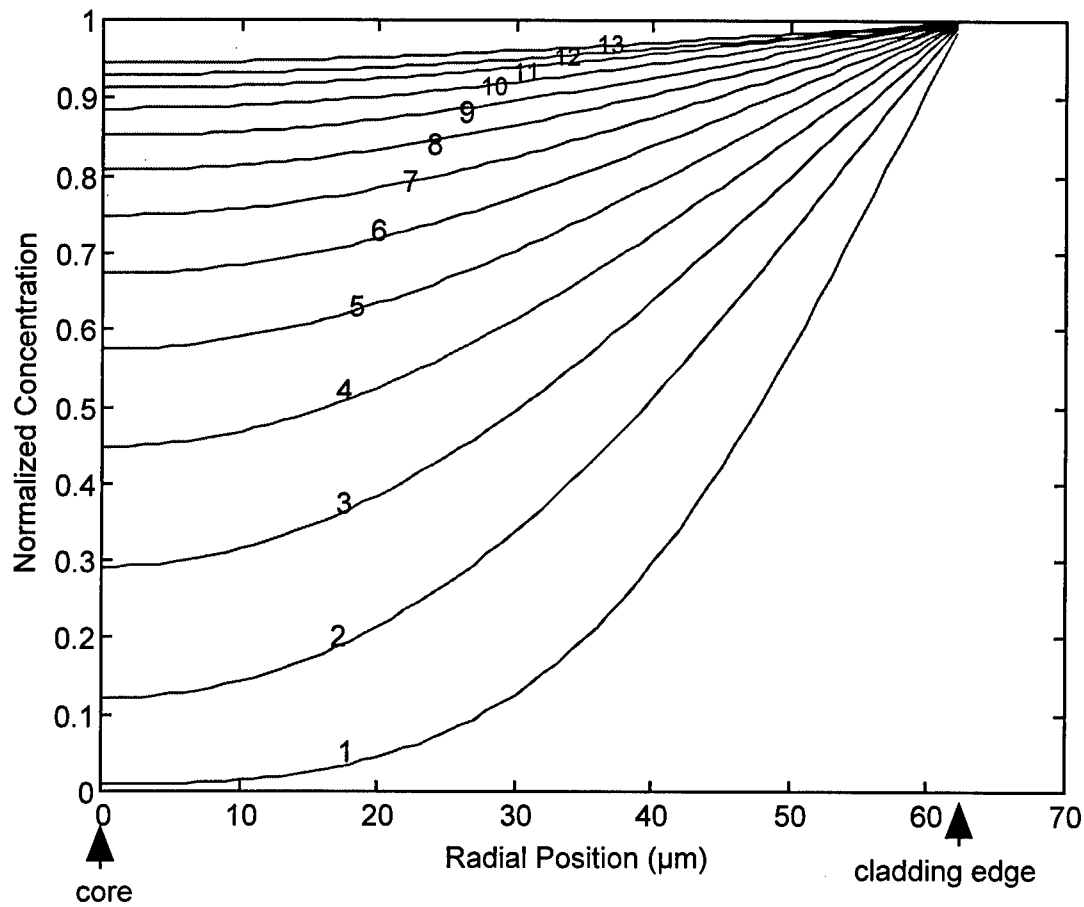


**Figure 3- 3** Normalized concentration of hydrogen gas diffused into the fiber as a function of radial position in the fiber. The multiple traces represent concentration vs. loading time labeled in days.

Fig. 3-3 presents a series of plots of the normalized hydrogen concentration versus radial position in the fiber at a temperature of 294 K. Multiple plots are used to illustrate how the hydrogen concentration in the fiber increases with time (measured in day increments.) At this temperature it takes approximately 13 days for the hydrogen concentration to reach 95% of its equilibrium value. This is more evident in Fig. 3-4 which presents the data in the form of concentration at the core versus time. Increasing the temperature at which the hydrogen is loaded into the fiber speeds the diffusion process and decreases the loading time. For example, elevating the temperature to 300 K reduces the loading time for a 95% normalized concentration to approximately nine days as shown in Fig. 3-4. Although increasing the temperature reduces the loading time, it also reduces the amount of hydrogen molecules which can be absorbed into the fiber, or solubility  $S$ . Solubility is inversely proportional to temperature and is given by [10],

$$S = 3.37 \exp(1041.66 / T) \text{ ppm/atm.} \quad 3-3$$

From Eqn. 3-3, increasing the temperature results in a lower total concentration of hydrogen in the fiber at a given pressure. However, a higher concentration can be obtained by the loading pressure. The equilibrium concentration of hydrogen at the core of the fiber is equal to the solubility times the loading pressure,

$$C_o = S \cdot P \text{ ppm.} \quad 3-4$$

Although greater concentrations can be obtained with increased pressure, the mechanical tolerances of the loading system impose a limit on the maximum pressure which can be used.

In addition to the obvious concerns of using a high pressure gas system, hydrogen gas is explosive, weakens the structure of metals over time, and can be volatile under pressure. Thus the optimal balance of pressure, temperature, and time is ultimately dependent upon the system used.

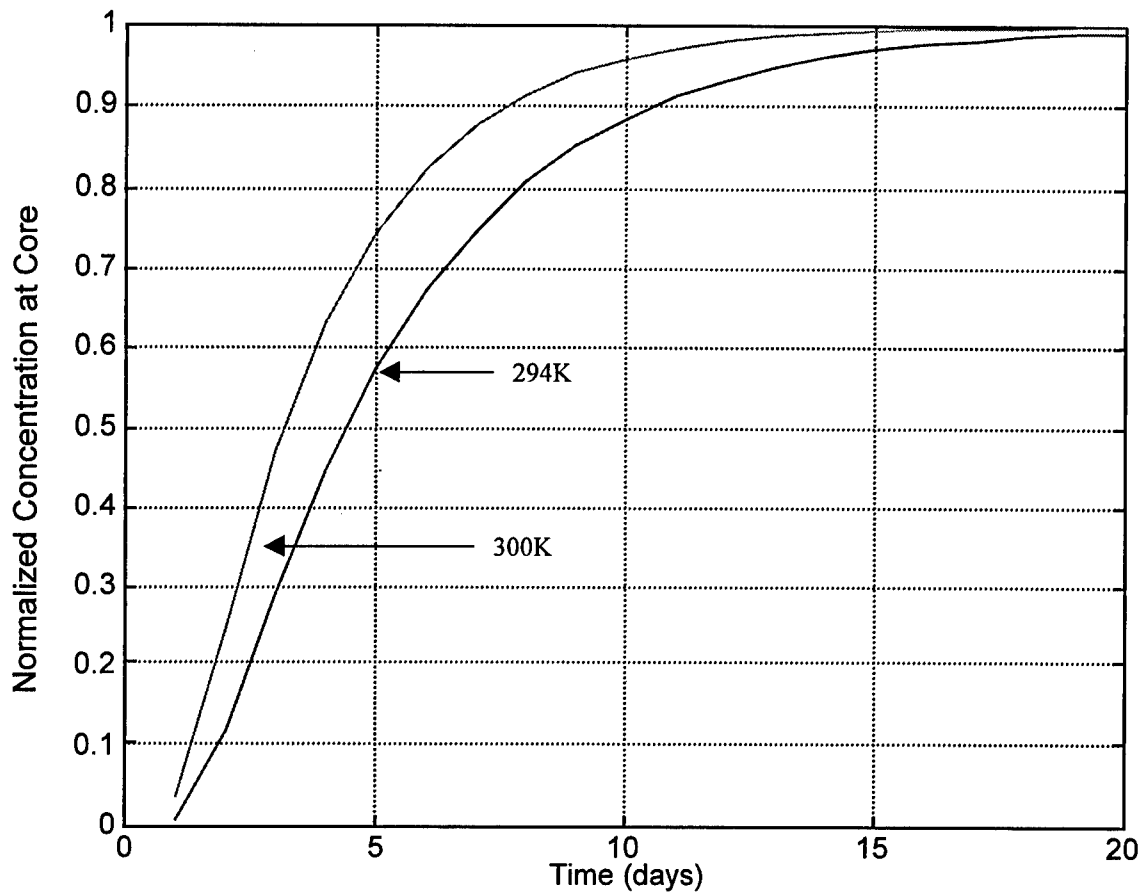


**Figure 3- 4** Normalized concentration of hydrogen in the core of the fiber as a function of time at 300 K and 294 K.

### 3.2.1 Hydrogen Loading System

A hydrogen loading system was designed and constructed to sensitize optical fibers as described above. The system, shown schematically in Fig. 3-5, consists of two functional sections, a loading assembly to house the fiber and a gas supply/delivery system to pressurize the loading assembly. The entire system is constructed from stainless steel pipes pressure rated for 7500 psi and high pressure Swagelok fittings. The weakest fitting is pressure rated for 3000 psi with a 4:1 safety ratio. The system is typically operated at 2000 psi, leaving a 1000 psi safety margin.

The loading assembly consists of a loading chamber which holds the fiber during loading and a water-based heat exchanger used to regulate the loading temperature. The loading chamber is simply a meter long stainless steel tube 0.25 inch in diameter. Fiber is spooled lengthwise on a rod and inserted and sealed inside this tube. The heat exchanger is formed by connecting a one inch diameter stainless steel tube between two one inch T-fittings. The smaller diameter loading chamber is centered inside this one inch wide assembly and connected to it at the ends of each tee via a reducing adapter. This creates a sealed space between the outside of the loading chamber and the inside of the T-fittings and pipe. The bottom of the T-fittings are used as a water inlet and outlet from this space to a temperature controlled water supply as shown in Fig. 3-5. Temperature regulated water is circulated in this space to maintain the temperature in the loading chamber at a desired value.

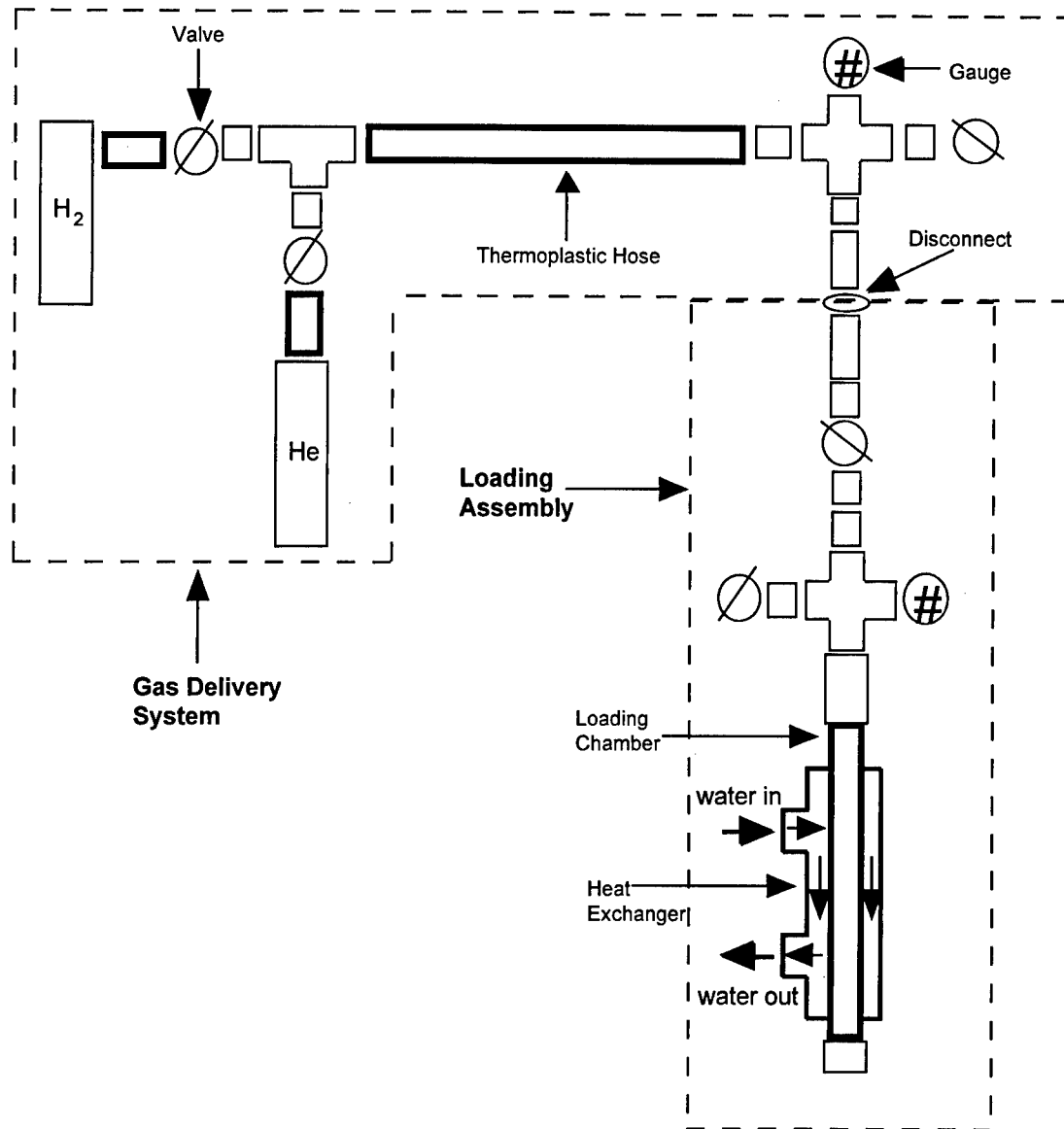


**Figure 3- 5** Schematic of the hydrogen loading system consisting of two functional parts, the gas delivery system and the loading assembly.

The gas supply system uses both hydrogen and helium source tanks. These tanks are connected via thermoplastic hoses (rated for 5000 psi) to a quick disconnect fitting. The quick disconnect allows the loading assembly to be pressurized and then disconnected, isolating the assembly from the hydrogen source.

Helium is used first to safety test the system. Unlike hydrogen it is not combustible, but like hydrogen it has a small atomic number which makes it a valid substitute for leak testing. The helium gas is gradually introduced into the system by increasing the supply pressure in steps, one section at a time, using various safety valves in the system. With each step increase in pressure leak tests are performed using both a high-pressure leak detector fluid and a helium "sniffer" (a mass-spectrometer to detect trace quantities of leaking helium). When the system is fully pressurized and verified to be leak free and safe, it is de-pressurized via a venting valve and then re-pressurized with hydrogen following the same steps.

The system is typically operated at 2000 psi to allow a 1000 psi safety margin for the weakest fitting in the system. From Eqn. 3-3, the equilibrium solubility of hydrogen in the fiber is approximately 116 ppm/atm at a temperature of 294 K. At a pressure of 2000 psi the core is loaded with 1.6 % hydrogen, a concentration which has experimentally proven to be adequate for writing strong gratings in most fibers.

### **3.3 Writing Techniques**

There are several different approaches to writing gratings in fiber. Fig. 3-6 summarizes the general techniques.

The phase mask technique is illustrated in Fig. 3-6a.<sup>13</sup> A phase mask is a silica substrate that has a grating pattern etched onto its surface. The plus/minus 1 diffracted orders (the zero order is typically suppressed) exiting an illuminated phase mask interfere to form a grating in a fiber placed behind the mask. The advantages of the phase mask technique are ease of use

for the mass production of gratings, easy alignment, reduced stability and coherence requirements compared to holographic techniques, and the ability to computer generate arbitrary interference profiles and chirped gratings. The main draw back to this technique is that a mask can produce a grating at only a single specific wavelength.

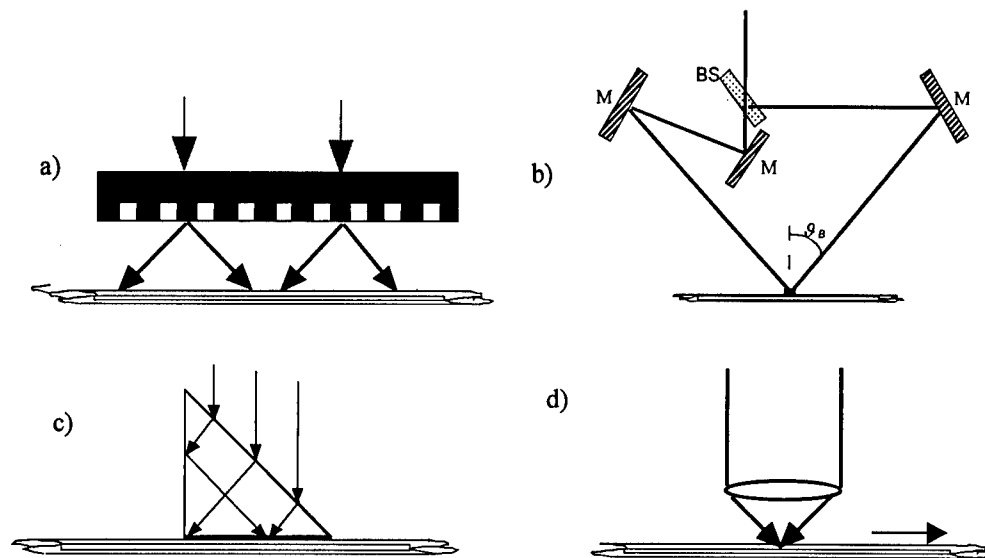


**Figure 3- 6** General methods used to create fiber gratings utilizing the side writing technique. They include a) phase mask technique, b) holographic technique, c) prism technique, and d) point by point method.

Thus there is an associated cost for making a new mask each time a grating at a different wavelength is needed.

Another common approach to writing fiber gratings is the holographic approach illustrated in Fig 3-6b. A two beam interference pattern is created by an interferometer and recorded in the

fiber. The main advantage of this approach is that the period of the interference pattern may be tuned to produce gratings that operate over a wide range of wavelengths. Coherence and stability requirements are the main difficulties encountered with this method. This approach is discussed in more detail in Section 3.4.

A variation of the holographic approach is the prism technique picture in Fig. 3-6c. The prism acts as a common path interferometer making it an inherently more stable arrangement. The illuminating laser beam is incident on the prism hypotenuse. This input is oriented so that half the beam is reflected off the back face of the prism and interferes with the other half of the beam that is refracted directly to the bottom of the prism. In essence, the grating is formed by folding a beam unto itself. One drawback to this approach is that the folded beam produces a "half Gaussian" index profile in the fiber which can create strong side lobes in the reflection spectrum.<sup>14</sup>

The final technique illustrated in Fig. 3-6d is the point by point writing method. A writing beam is pulsed as the fiber is translated so that the individual grating lines may be written into the fiber. The input beam must thus be tightly focused. Also, the process is slow and requires high precision translation.

### **3.4 Reflection Fiber Gratings**

In this section, the fabrication of unslanted reflection fiber Bragg gratings is discussed.

Gratings are formed using the holographic methods as discussed below.



### 3.4.1 Grating Period Calculation

In general, diffraction from a periodic structure can be described by the grating equation,

$$n \sin \theta_2 = n \sin \theta_1 + \frac{m\lambda}{\Lambda} \quad 3-5$$

where  $\theta_1$  is the angle of incidence of a wave on the grating,  $\theta_2$  is the angle of the diffracted wave,  $\Lambda$  is the grating period, and  $m$  is the order of diffraction. The grating equation expresses the phase matching condition that results from the boundary conditions imposed by Maxwell equations. For each diffraction order, it predicts where energy will be scattered and at what wavelength constructive interference from the scattering point occurs. For the special case when the incidence angle equals the angle of diffraction, the Bragg condition is satisfied and resonant coupling of energy can occur.

The grating equation may be applied to the problem of diffraction from a fiber grating by recognizing that the mode propagation constant  $\beta$  is equal to  $kn_{\text{eff}}$  and that  $n_{\text{eff}} = n_{\text{core}} \sin \theta$ .

Substituting these equalities into Eqn. 3-5 yields,

$$k_2 n_{\text{eff}} = k_1 n_{\text{eff}} + \frac{2\pi m}{\Lambda}, \quad 3-6$$

or,

$$\lambda = (n_{\text{eff}1} + n_{\text{eff}2})\Lambda. \quad 3-7$$

Assuming a non-slanted reflection fiber grating in single mode fiber that couples a forward going  $\text{LP}_{01}$  mode to a backward propagating  $\text{LP}_{01}$  mode,  $n_{\text{eff}1} = n_{\text{eff}2}$  and Eqn. 3-7 becomes,

$$\Lambda = \frac{\lambda}{2n_{eff}}, \quad 3-8$$

which is the Bragg condition.

Eqn. 3-6 may be expressed pictorially in the form of a Bragg Diagram. The diagram provides a convenient approach to calculating the grating period, the angle of diffraction, and the interbeam angle between the writing beams when they are at a different wavelength than the signal beam. Fig. 3-7 is an example of a Bragg diagram for the case of an unslanted reflection grating. In the figure,  $K$  represents the grating vector,  $k_w$  is the wavevector of the write beams, and  $k_s$  is the wavevector of the signal beams. Again assuming a single mode fiber and coupling of a forward going  $LP_{01}$  mode to a backward propagating  $LP_{01}$  mode, the magnitude of the  $k$  vectors are both equal. By simple addition of the  $k$  vectors in the diagram, the grating vector is found to be,

$$K = 2k_s n, \quad 3-9$$

or,

$$\Lambda = \frac{\lambda_s}{2n}. \quad 3-10$$

To form a grating with this period the writing wavelength and geometry must be taken into consideration. The desired wavelength of operation of a grating is typically different from the wavelength used to write the grating and thus the lengths of  $k_w$  and  $k_s$  will be different (the most commonly used propagation wavelengths are 1300 nm and 1550 nm while the grating is written at 244 nm.) As a result, the interbeam angle formed between the grating vectors of the writing beams and that of the signal beams must thus be different if Bragg matching is to be

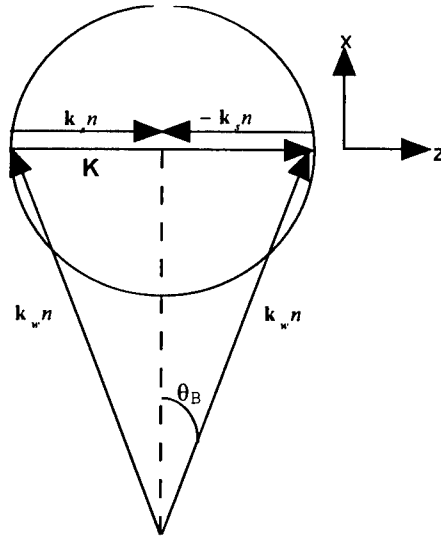


**Figure 3- 7** Bragg diagram for a non-slanted reflection grating.

achieved. Pictorially, the interbeam angle (in the fiber) between writing beams with wavelength  $\lambda_w$  needed to achieve Bragg matching at a signal wavelength  $\lambda_s$  is equal to the angle formed by  $k_w$  and the perpendicular bisector of  $K$ . From the diagram,

$$\theta_B = \sin^{-1} \left( \frac{\frac{K}{2}}{k_w n} \right) = \sin^{-1} \left( \frac{\lambda_w}{2\Lambda n} \right). \quad 3-11$$

### 3.4.2 Experimental Setup

The experimental setup used for fabricating reflection type fiber gratings is similar to a basic Mach-Zehnder interferometer and is illustrated in Fig. 3-8. The 244 nm wavelength laser energy necessary for writing gratings in fiber is produced by an intracavity frequency doubled

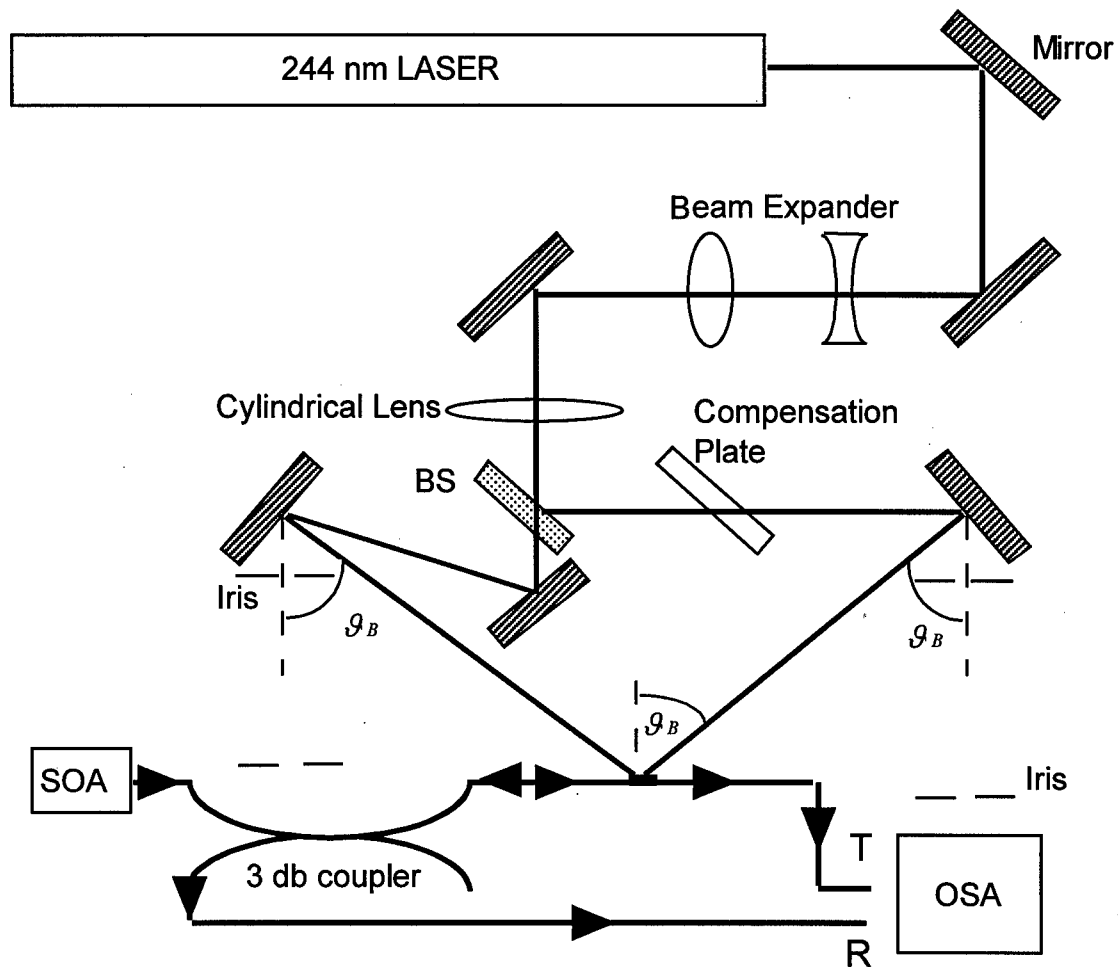


**Figure 3- 8** Experimental setup used for producing reflection fiber Bragg gratings.

Argon-ion laser (Coherent model FRED). Light from the laser is expanded using a simple Galilean telescope and is directed to a beam splitter using a series of UV mirrors. The light is then split along two paths which are later recombined at the fiber.

The path lengths of the interferometer were equalized within the coherence length of the laser. A UV grade fused silica compensation plate was inserted in one arm of the interferometer to balance the mismatch in optical path lengths between the two arms created by the beam splitter. Also, an additional mirror was added to one arm of the interferometer to allow the beams in both arms to undergo the same number of reflections and have similar portions of the two wavefronts interfere with each other in the fiber plane.

A cylindrical lens is used to focus both beams along the axis of the fiber core. This produces a greater intensity interference pattern on the core and reduces exposure time. Typically the cylindrical lens is placed before the beam splitter. This eases alignment and allows both arms of the interferometer to focus the beam at the same place. This approach works well for hydrogen loaded fibers. For the case where the fiber is not hydrogen loaded and/or photo-sensitivity is decreased, a separate cylindrical lens of a shorter focal length is used in each arm of the interferometer. A shorter focal length lens positioned directly in front of the fiber produces a smaller spot size on the fiber and results in greater exposure energy at the core.

The two turning mirrors in the interferometer determine the Bragg angle,  $\theta_B$ , and the period of the grating (Eqn. 3-11). Both mirrors are mounted on precision motorized rotational stages

with  $.001^\circ$  angular resolution. These stages allow precise adjustment of the Bragg angle for tuning of the grating wavelength. To obtain the proper Bragg angle, a reference position is first set. The tuning mirror of each arm is positioned to reflect the light coming from the beam splitter through a set of centered irises (Fig. 3-8). The light is thus reflected along a path that is parallel to the normal of the fiber. From this position, the mirrors are then moved by an angle  $\theta_B / 2$  (since the reflection angle off a mirror is  $2\theta$ ) to produce a beam intersection angle of  $\theta_B$  with the fiber normal (as shown by the alternate interior angles in Fig. 3-8.)

The focused beams intersecting on the fiber must be carefully aligned so that they overlap and focus in the core region. Two methods are used to aid in this alignment. The first is to use the scattering of UV light off the fiber to help determine the orientation of the cylindrical lens. Scattering patterns have been studied in depth by Presby and Marcuse to help measure fiber uniformity and index during fiber manufacture.<sup>15 16</sup> Here these patterns are used to determine the best placement of the cylindrical lens with respect to the fiber. A UV sensitive screen is placed behind the fiber to capture both writing beams after they diverge from the fiber. The fiber produces a diffraction pattern and a shadow of itself in both beams. While viewing these patterns on the screen, the height of the cylindrical lens is adjusted until the shadow is centered in the diffraction pattern. Any tilt/rotation introduced by misalignment of the cylindrical lens is then adjusted by rotating the cylindrical lens until the sinc-like diffraction patterns are parallel to the fiber and the shadow region. The size of the shadow region

compared with the entire beam profile also provides a rough estimate of the proper placement of the fiber with respect to the focal plane of the lens.

The second alignment technique is based on the fluorescence in the 400 nm region the fiber produces when irradiated with light at 244 nm [14]. As the light is focused down tighter on the fiber, this fluorescence increases. This is thus used to position the lens so that it focuses the light in the fiber plane. The blue fluorescence escaping out the end of the fiber is measured with an optical power meter and the optimal fiber position may be determined when the measurement is peaked. These two alignment techniques may thus be combined to provide course and fine adjustment of the cylindrical lens with respect to the fiber.

Since the typical period of a reflection fiber grating is on the order of  $0.5\text{ }\mu\text{m}$  or less (Eqn. 3-6), system stability and vibration isolation are important issues. Hence all the components in the interferometer are mounted as low to the optical table as possible for greater fringe stability. A Plexiglas case also covers the interferometer to isolate the setup from air currents. As a check on stability, a Michelson interferometer using a HeNe laser was constructed within the Plexiglas box. The fringes from this interferometer are projected onto a screen and fringe movement is monitored to indicate any instability.

A fiber grating is typically measured in-situ as it is being written using a broadband source and an optical spectrum analyzer (OSA). The spontaneous emission from a semiconductor optical amplifier (SOA) is used as the broadband source in these experiments (Fig. 3.9.) Prior to exposure, light from the SOA is coupled into the fiber and then back out into the OSA

(Ando model AQ-6315B with a maximum 0.05 nm resolution.) With this configuration, changes in the power spectra of the SOA caused by the formation of a grating are observed on the OSA during exposure. These changes indicate the wavelength of operation, the bandwidth, and the strength of the grating being formed. Gratings of any desired reflectivity can be produced by simply terminating the exposure when the grating strength reaches the desired value. By using a 3 dB coupler as shown in Fig. 3-7, a grating can be viewed either in transmission or reflection on the OSA.

### **3.4.3 Experimental Results**

In this section experimental grating data is presented for unslanted fiber Bragg gratings. Common to all of the data provided is the measurement technique. The data is recorded using the OSA configured to measure the transmission of the SOA through a fiber during exposure. Fig. 3-9 is a reference of the power spectra for a 1500 nm SOA with no grating present. In the data below, the gratings in the 1550 nm region appear as a notch in this spectrum. SOAs centered at 1300 and 800 nm were also used to write gratings in these respective wavelength ranges. Their spectra are similar in shape and bandwidth to that of Fig. 3-9.



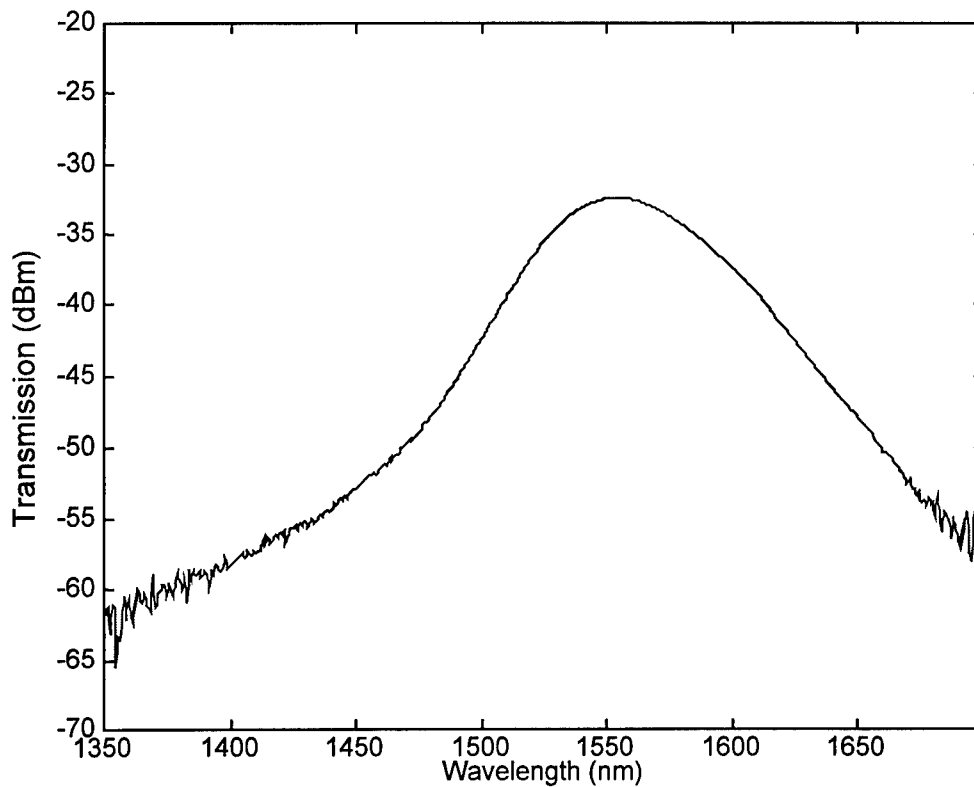


**Figure 3- 9** Transmission spectrum of a 1550 nm SOA used as a broadband source to measure fiber gratings.

### 3.4.3.1 Uniform Grating

As discussed in Section 2.3.2, a uniform grating has a sinusoidal index modulation with a constant, or uniform, average index. To form such a grating, spatially uniform writing beams are required. The writing beams produced by the laser, however, have a Gaussian profile. A uniform grating is thus created by first expanding the laser beams and then placing an adjustable slit in each arm of the interferometer. The slit is used to limit each beam to a 0.8 mm diameter spot of uniform intensity. Experimental data is given in Fig. 3-10 for a uniform

grating formed in this way in hydrogen loaded Corning SMF-28 single mode fiber. Also included in the figure is the calculated theoretical spectrum obtained from using the coupled mode theory of Section 2.3.2.

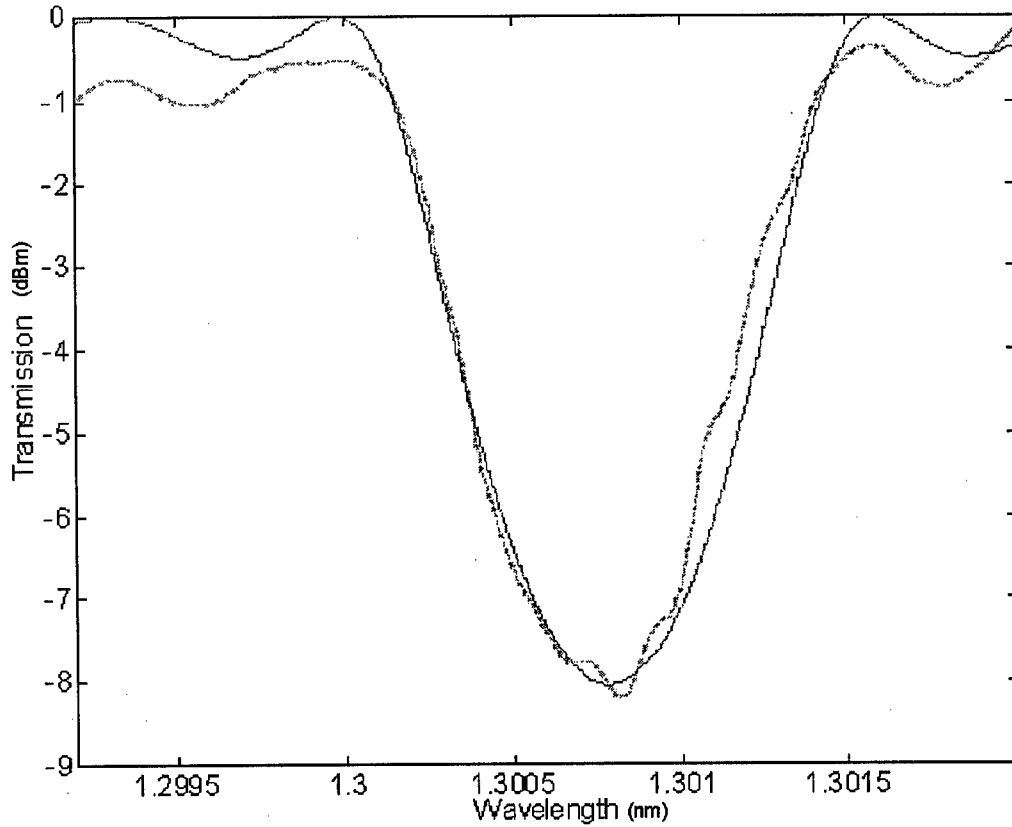


**Figure 3- 10** Measured and calculated transmission spectra for Bragg reflection in a 0.8 mm long uniform grating with  $\kappa L = 1.577$ .

To perform the theoretical calculation, the coupling constant of the grating can be determined with the aid of Eqn. 2-62,

$$R_{\max} = \tanh^2(\kappa L), \quad 3-12$$

using the known length of the grating and experimentally measured peak reflectivity.

Once  $\kappa$  is determined, it may be substituted into Eqn. 2-56,

$$R = \frac{(\kappa L)^2 \sinh^2(\sqrt{(\kappa L)^2 - (\delta L)^2})}{(\kappa L)^2 \cosh^2(\sqrt{(\kappa L)^2 - (\delta L)^2}) - (\delta L)^2} \quad 3-13$$

and the theoretical spectrum can be calculated as a function of wavelength.

Since the grating is uniform, it is expected that the peak of the grating will coincide with the Bragg wavelength at the center of the grating. Indeed, in Fig. 3-10, the experimental peak reflectivity occurs at the center wavelength 1300.785 nm. The measured peak of approximately 8 dB at this wavelength yields a value of  $\kappa L = 1.577$ , or  $\Delta n = 8.136 \times 10^{-4}$  using Eqn. 3-12. Substituting this value of  $\kappa L$  in Eqn. 3-13, a reasonable fit to the measured data is obtained. As another check, Eqn. 2.59 predicts a grating bandwidth of  $.0012(\lambda_B)$  for this case or 1.56 nm. This is very close to the approximate 1.5 nm bandwidth of the measured data as shown in Fig. 3-10.

### 3.4.3.2 Non-uniform Grating

Gratings with a non-uniform index profile described in Section 2.3.3 were also written. These gratings had a Gaussian index profile formed with beams approximately 4 mm in diameter.

An example grating formed in hydrogen loaded Corning SMF-28 is given in Fig. 3-11.

Notice that as expected, this grating is no longer symmetric like the uniform grating in Fig. 3-

10. The grating reflectivity for this case is at least 30 dB, the measurement limited by the

signal strength of the SOA and the noise floor of the OSA. Also evident are the Fabry-Perot resonances on the short wavelength side of the grating that were predicted and discussed in Chapter 2. Fig. 3-12 is a plot of the calculated spectrum a 4 mm long Gaussian profile grating with  $\sigma = 7 \times 10^{-4}$ . The plot is similar in structure and strength to the experimental data and to first order provides a reasonable match.

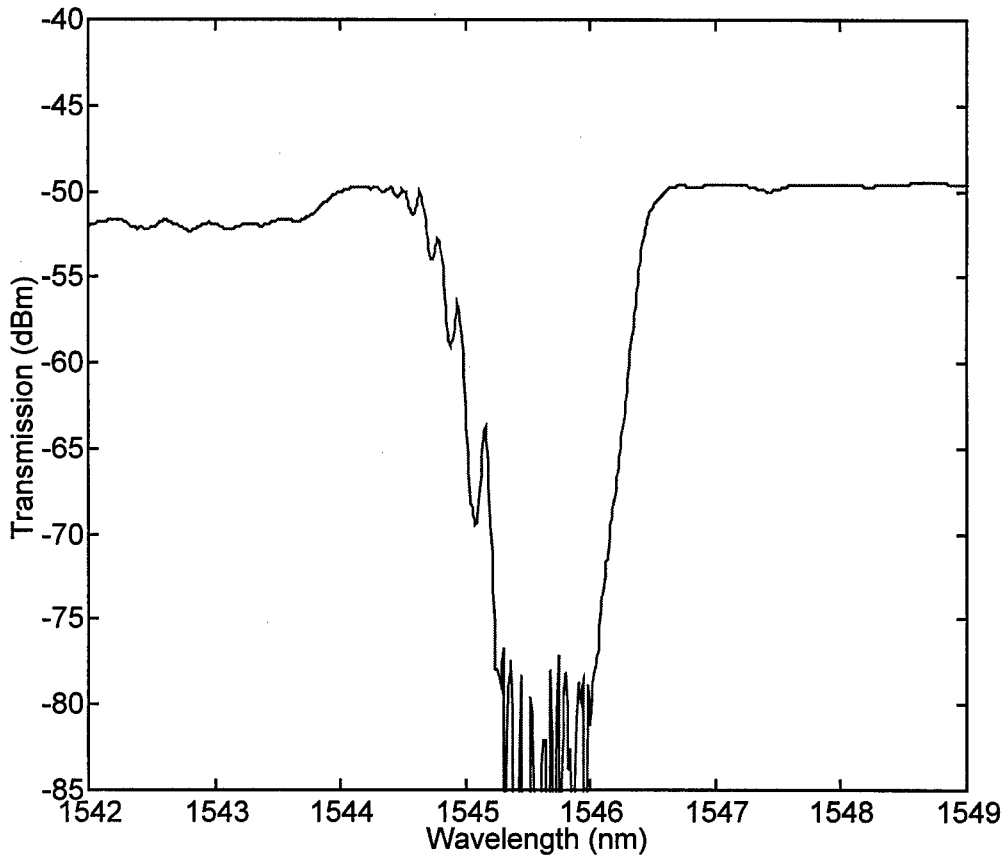


**Figure 3- 11** Measured transmission spectrum of a 4 mm long fiber Bragg reflection with a Gaussian profile. Fabry-Perot resonances are present on the short wavelength side of the grating. The measured transmission of the grating is limited by the 80 dB noise floor of the OSA.

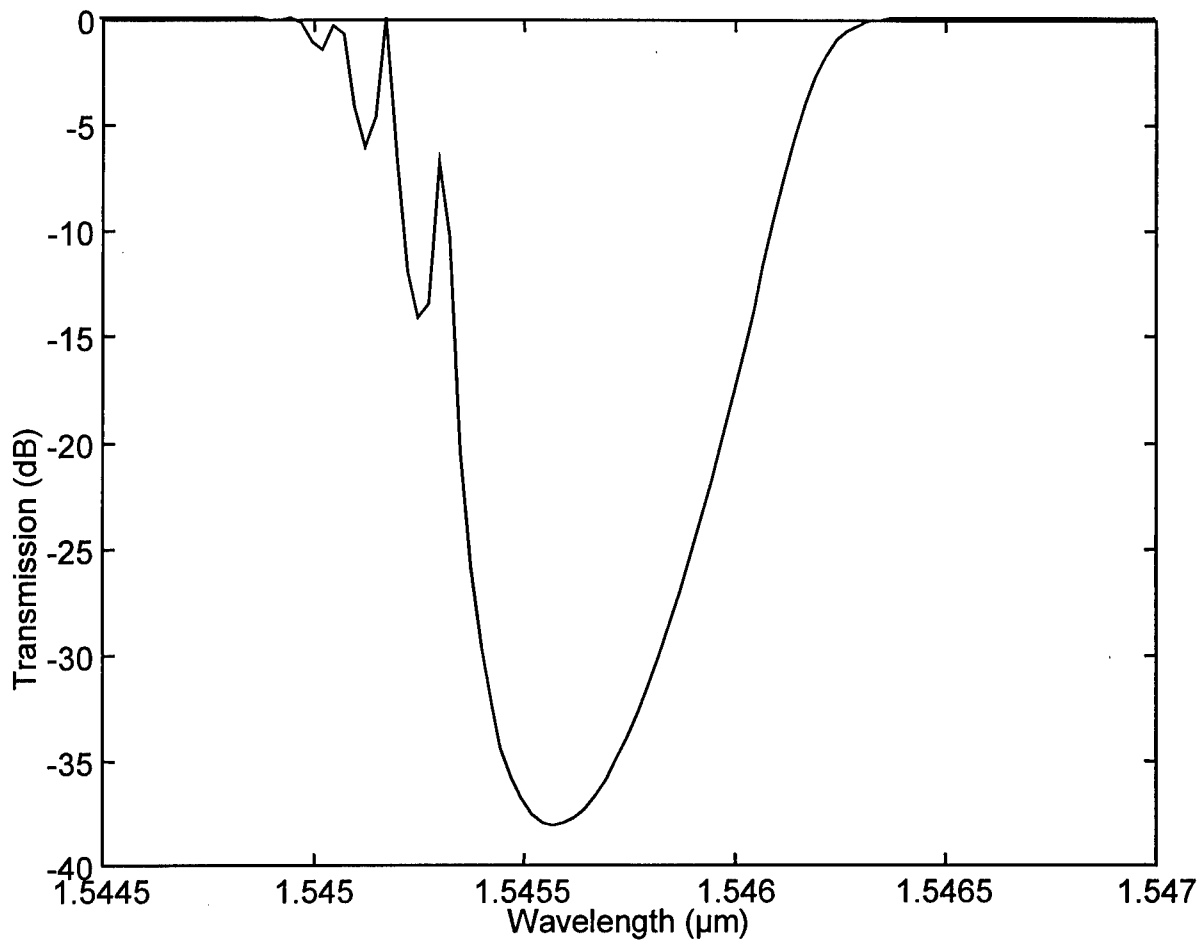


**Figure 3- 12** Calculated transmission spectrum of a 4 mm FWHM Gaussian index profile grating with  $\sigma = 7 \times 10^{-4}$ ,  $\Delta = .004$ , and  $n_{\text{clad}}=1.447$ .

It was also predicted in Chapter 2 that the average index of a non-uniform grating increases with exposure shifting the center Bragg wavelength. Fig. 3-13 illustrates this with a grating written in hydrogen loaded QPS fiber (QPS-PFBG-1355-T) that was measured at two different times (4 minutes apart) during exposure. Not only does the center wavelength shift, but as the index modulation increases over time, the grating bandwidth increases as predicted by Eqn. 2-61 for a strong grating. The grating reflectivity is also greatly enhanced with increased index as expected.

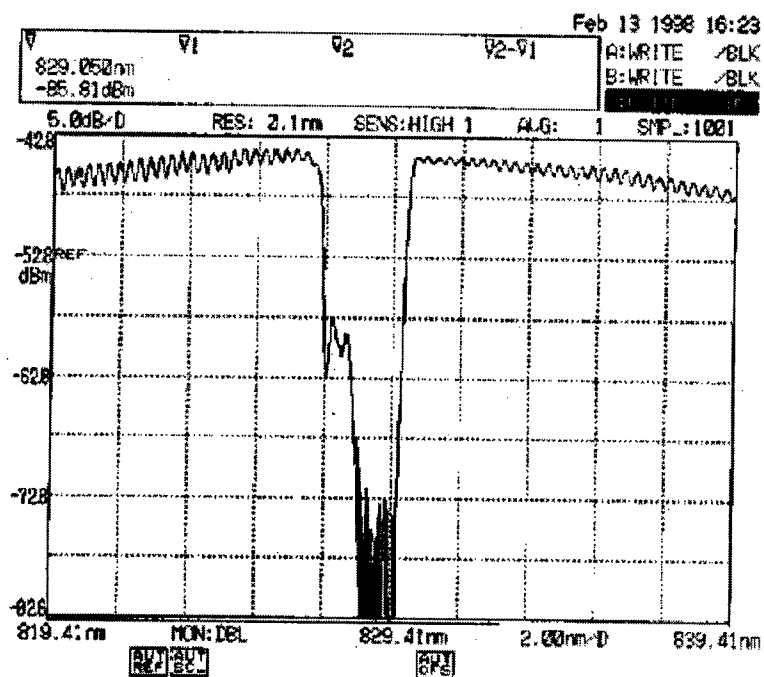
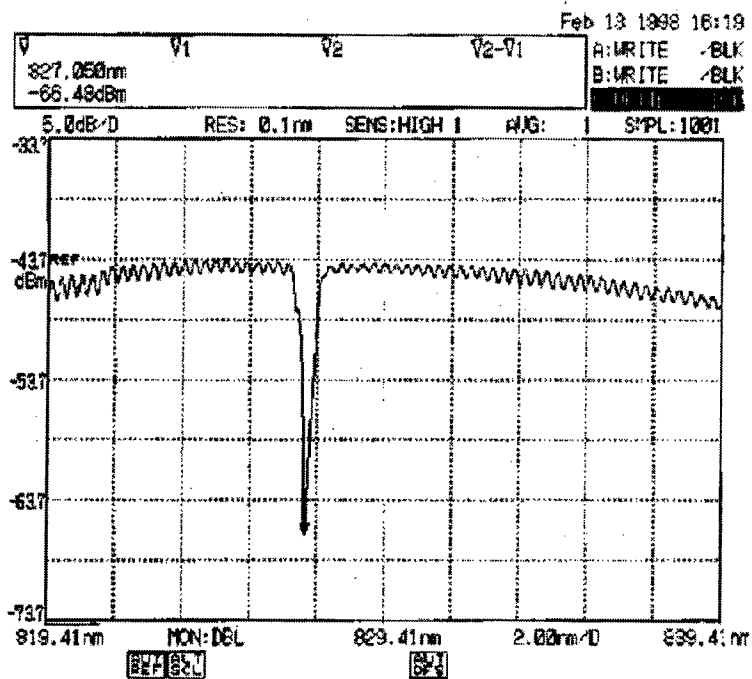


**Figure 3- 13** Shift in center wavelength of fiber grating from 827 nm to 829 nm with exposure time.

### **3.5 Summary**

The basics of fiber grating formation were given in this chapter. This included a discussion on a current theory used to explain photosensitivity as well as the effects of hydrogen loading on the process. The experimental apparatus used to load fibers and write gratings was presented. Experimental results for fiber gratings were given and compared to theory.

- <sup>1</sup> H. Hosono, Y. Abe, D. L. Kinser, R. A. Weeks, K. Muta, and H. Kawazoe, "Nature and origin of the 5 eV band in  $\text{SiO}_2\text{-GeO}_2$  glasses," *Phys. Rev. B.*, vol. 46, pp. 11445-11451, 1992.
- <sup>2</sup> L. N. Skuja, A. N. Trukhin, A. E. Plaudis, " Luminescence in germanium-doped glassy  $\text{SiO}_2$ ," *Phys. Stat. Solid A.*, vol. 84, pp. K153-157, 1984.
- <sup>3</sup> R. M. Atkins, V. Mizrahi, and T. Erdogan, " , " *Electron Lett.*, vol 28 pp. Xxxxx 1993.
- <sup>4</sup> D. P. Hand and P. St. J. Russell, "Photoinduced refractive-index changes in germanosilicate fibers," *Opt. Lett.*, vol. 15, pp. 102-104, 1990.
- <sup>5</sup> E. J. Friebele and D. L. Griscom, in *Proceedings of the Materials Research Society Symposium* (Materials Research Society, Pittsburgh, PA, 1986) p. 319.
- <sup>6</sup> G. P. Agrawal, *Nonlinear Fiber Optics*, (Academic Press, San Diego, 1995.)
- <sup>7</sup> L. Dong, J. L. Archambault, L. Reekie, P. St. J. Russel, and D. N. Payne, "Photoinduced absorption change in germanosilicate preforms: evidence for the color-center model of photosensitivity," *Appl. Opt.*, vol. 34, pp. 3436-3440, 1995.
- <sup>8</sup> T. Ergogan and V. Mizrahi, "Fiber Phase Gratings Reflect Advances in Lightwave Technology," *Laser Focus World*, pp. 75-80, February 1994.
- <sup>9</sup> P. J. Lemaire, R. M. Atkins, V. Mizrahi, and W. A. Reed, "High pressure  $\text{H}_2$  loading as a technique for achieving ultrahigh UV photosensitivity and thermal sensitivity in  $\text{GeO}_2$  doped optical fibers," *Electron. Lett.*, vol. 29, pp. 1191-1193, 1993.
- <sup>10</sup> V. Mizrahi, P. J. Lemaire, T. Erdogan, W. A. Reed, D. J. DiGiovanni, R. M. Atkins, "Ultraviolet laser fabrication of ultrastrong optical fiber gratings and of germania-doped cannel waveguides," *Appl. Phys. Lett.*, 63, pp. 1727-9, 1993.
- <sup>11</sup> J. Crank, *The Mathematics of Diffusion*, (Oxford University Press, London, 1975) pp. 69-74.
- <sup>12</sup> P. J. Lemaire, "Reliability of optical fibers exposed to hydrogen: prediction of long-term loss increases," *Opt. Eng.*, vol. 30, pp. 780-789, 1991.
- <sup>13</sup> K. O. Hill, B. Malo, F. Bilodeau, D. C. Johnson, J. Albert, "Bragg gratings fabricated in monomode photosensitive optical fiber by UV exposure through a phase mask," *Appl. Phys. Lett.*, vol. 62, pp. 1035-1037, 1993
- <sup>14</sup> H. Patrick, and S. L. Gilbert, "Growth of Bragg gratings produced by continuous-wave ultraviolet light in optical fiber," *Opt. Lett.*, vol. 18, pp. 1484-1486, 1993.
- <sup>15</sup> H. M Presby, "Refractive index and diameter measurements of unclad fibers," *J. Opt. Soc. Am.*, vol. 64, pp. 280-284, 1974.
- <sup>16</sup> D. Marcuse and H. M Presby, "Light scattering from optical fibers with arbitrary refractive-index distributions," *J. Opt. Soc. Am.*, vol. 65, pp. 367-375, 1975.



## **Chapter 4: Conclusion**

### **4.1 Summary**

It has been the focus of this project to study fiber Bragg gratings and develop an in-house capability to model and fabricate them.

Waveguide and fiber concepts were discussed at the start of this report to provide a foundation for understanding how fiber based grating devices function. To this end, coupled mode theory was used to model reflection fiber gratings. The effects of experimental parameters on grating characteristics were modeled for both uniform and non-uniform grating profiles using this approach.

Fabrication of gratings in standard communication single mode fiber required an enhancement of the fiber's photosensitivity by way of high-pressure hydrogen treatment. The theory behind this technique as well as the experimental system used to treat the fibers was discussed. Once treated, the fibers were fabricated using a holographic approach. The performance of gratings fabricated by this method was then compared to theoretical predictions and was found to be in good agreement.

Fiber grating show great potential for use in RF photonic systems. Other in-house efforts are currently examining the use of fiber gratings in phased array radar beam steering systems.